D5.1 Advanced and Reliable Models for Natural and Man-Made Hazards

Deliverable number	**D5.1.**
Deliverable title	Advanced and Reliable Models for Natural and Man-Made Hazards
Nature[1]	**R**
Dissemination Level [2]	**PU**
Author (email) Institution	**George Efthimiou (gefthimiou@meng.auth.gr), Fotios Barmpas (fotisb@auth.gr), AUTH** **Dimitrios Vamvatsikos (divamva@mail.ntua.gr) (NTUA)**
Editor (email) Institution	**Antonis Kalis (antonis.kalis@iccs.gr)** **ICCS**
Leading partner	**AUTH**
Participating partners	**ALL**

[1] **R**=Document, report; **DEM**=Demonstrator, pilot, prototype; **DEC**=website, patent fillings, videos, etc.; **OTHER**=other

[2] **PU**=Public, **CO**=Confidential, only for members of the consortium (including the Commission Services), **CI**=Classified, as referred to in Commission Decision 2001/844/EC

Official submission date:	**27/05/2021**
Actual submission date:	**07/06/2021**

Modifications Index

Date	Version
25/01/2021	0.1
26/01/2021	0.2
27/05/2021	0.3
31/05/2021	0.4
3/06/2021	0.5
7/06/2021	0.6

This work is a part of the HYPERION project. HYPERION has received funding from the European Union's Horizon 2020 research and innovation programme under grant agreement no 821054.

ACRONYMS AND ABBREVIATIONS

ARPS	Advanced Region Prediction System
CAM	Community Atmosphere Model
DEM	Digital Elevation Model
FFT	Fast Fourier transform
GEM	Global Environmental Multiscale Model
GFS	Global Forecast System
HIRLAM	High Resolution Limited Area Model
IGCM	Intermediate General Circulation Model
LAMs	Limited-area models
LCM	Lagrangian cloud model
LPM	Lagrangian particle model
MOS	Model output statistics
MOST	Monin-Obukhov similarity theory
MPI	Max-Planck-Institute & Message Passing Interface
MSC	Meteorological Service of Canada
NAM	North American Mesoscale model
NCAR	National Center for Atmospheric Research
NWP	Numerical weather prediction
OML	Ocean mixed layer

RAMS	Regional Atmospheric Modelling System
SGS	Subgrid-scale
TKE	Turbulent kinetic energy
UAM	Urban Airshed Model
UM	Unified Model
WRF	Weather Research and Forecasting model
WRF-ARW	Advanced Research WRF
WRF-NMM	WRF Nonhydrostatic Mesoscale Model

Table of Contents

Executive Summary

Deliverable 5.1 presents advanced and reliable modelling for a broad spectrum of natural and man-made hazards as pertinent to the four pilot sites of HYPERION in Rhodes, Granada, Venice and Tonsberg, and provides the involved stakeholders, scientists and users useful information for their specific needs in handling natural and human induced disasters. Models were implemented by AUTH, with the assistance of FMI, RG and NTUA, building on existing research capacity in a broad spectrum of modelling approaches to natural and man-made hazards. Models of climatic impact are described based on environmental parameters (according to a reliability-based approach for durability) in order to define the needed parameters for the modeling purpose.

Legal Disclaimer

1. Introduction

1.1 Purpose of the Document

The document aims to present advanced and reliable modelling for a broad spectrum of natural and man-made hazards, and to provide the involved stakeholders, scientists and users with useful information for their specific needs in handling natural and human induced disasters. The work is based on existing research capacity in a broad spectrum of modelling approaches to natural and man-made hazards. The models include the atmospheric models and the seismic models.

1.2 Interpretation of the DoW

In D.5.1 we only deal with hazards/load models that are relevant to our HYPERION pilots, as these were defined in the work of WP2.

1.3 Intended audience

D.5.1 is a public document. It will be reachable by all stakeholders, Members of the Consortium and the Commission Services. It is particularly interesting for end users, i.e., agencies involved in the resilience and reconstruction of historic areas. The HYPERION system can assist their educational purposes and address additional requirements.

1.4 Structure of the deliverable

The document is structured in four chapters:

- Chapter 1 is this introduction.
- Chapter 2 describes the atmospheric models and the PALM model that was used in Working Package 3 (WP3) of the HYPERION project.
- Chapter 3 describes the seismic models.
- Chapter 4 presents the conclusions of the report.

2. Atmospheric models

2.1 General

A model is a computer program that produces meteorological information for future times at given locations and altitudes. Within any model is a set of equations, known as the primitive equations, used to predict the future state of the atmosphere [1]. These equations are initialized from the analysed data and rates of change are determined. These rates of change predict the state of the atmosphere a short time into the future, with each time increment known as a time step. The equations are then applied to this new atmospheric state to find new rates of change, and these new rates of change predict the atmosphere at a yet further time into the future. Time stepping is repeated until the solution reaches the desired forecast time. The length of the time step chosen within the model is related to the distance between the points on the computational grid, and is chosen to maintain numerical stability [2]. Time steps for global models are on the order of tens of minutes [3], while time steps for regional models are between one and four minutes [4]. The global models are run at varying times into the future. The UKMET Unified model is run six days into the future [5], the European Centre for Medium-Range Weather Forecasts model is run out to 10 days into the future [6], while the Global Forecast System model run by the Environmental Modelling Center is run 16 days into the future [7].

The equations used are nonlinear partial differential equations, which are impossible to solve exactly through analytical methods [8], with the exception of a few idealized cases [9]. Therefore, numerical methods obtain approximate solutions. Different models use different solution methods: some global models use spectral methods for the horizontal dimensions and finite difference methods for the vertical dimension, while regional models and other global models usually use finite-difference methods in all three dimensions [8]. The visual output produced by a model solution is known as a prognostic chart, or prog [10].

2.2 Types

The main assumption made by the **thermotropic** model is that while the magnitude of the thermal wind may change, its direction does not change with respect to height, and thus the baroclinicity in the atmosphere can be simulated using the 500 mb and 1,000 mb geopotential height surfaces and the average thermal wind between them [11-12].

Barotropic models assume the atmosphere is nearly barotropic, which means that the direction and speed of the geostrophic wind are independent of height. In other words, no vertical wind shear of the geostrophic wind. It also implies that thickness contours (a proxy for temperature) are parallel to upper-level height contours. In this type of atmosphere, high- and low-pressure areas are centers of warm and cold temperature anomalies. Warm-core highs (such as the subtropical ridge and Bermuda-Azores high) and cold-core lows have strengthening winds with height, with the reverse true for cold-core highs (shallow arctic highs) and warm-core lows (such as tropical cyclones) [13]. A barotropic model tries to solve a simplified form of

atmospheric dynamics based on the assumption that the atmosphere is in geostrophic balance; that is, that the Rossby number of the air in the atmosphere is small [14]. If the assumption is made that the atmosphere is divergence-free, the curl of the Euler equations reduces into the barotropic vorticity equation. This latter equation can be solved over a single layer of the atmosphere. Since the atmosphere at a height of approximately 5.5 kilometres is mostly divergence-free, the barotropic model best approximates the state of the atmosphere at a geopotential height corresponding to that altitude, which corresponds to the atmosphere's 500 mb pressure surface [15].

Hydrostatic models filter out vertically moving acoustic waves from the vertical momentum equation, which significantly increases the time step used within the model's run. This is known as the hydrostatic approximation. Hydrostatic models use either pressure or sigma-pressure vertical coordinates. Pressure coordinates intersect topography while sigma coordinates follow the contour of the land. Its hydrostatic assumption is reasonable as long as horizontal grid resolution is not small, which is a scale where the hydrostatic assumption fails. Models that use the entire vertical momentum equation are known as **nonhydrostatic**. A nonhydrostatic model can be solved anelastically, meaning it solves the complete continuity equation for air assuming it is incompressible, or elastically, meaning it solves the complete continuity equation for air and is fully compressible. Nonhydrostatic models use altitude or sigma altitude for their vertical coordinates. Altitude coordinates can intersect land while sigma-altitude coordinates follow the contours of the land [16].

2.3 History

The history of numerical weather prediction began in the 1920s through the efforts of Lewis Fry Richardson who utilized procedures developed by Vilhelm Bjerknes [17-18]. It was not until the advent of the computer and computer simulation that computation time was reduced to less than the forecast period itself. ENIAC created the first computer forecasts in 1950 [15, 19], and more powerful computers later increased the size of initial datasets and included more complicated versions of the equations of motion [20]. In 1966, West Germany and the United States began producing operational forecasts based on primitive-equation models, followed by the United Kingdom in 1972 and Australia in 1977 [17, 21]. The development of global forecasting models led to the first climate models [22-23]. The development of limited area (regional) models facilitated advances in forecasting the tracks of tropical cyclone as well as air quality in the 1970s and 1980s [24-25].

Because the output of forecast models based on atmospheric dynamics requires corrections near ground level, model output statistics (MOS) were developed in the 1970s and 1980s for individual forecast points (locations) [26-27]. Even with the increasing power of supercomputers, the forecast skill of numerical weather models only extends to about two weeks into the future, since the density and quality of observations—together with the chaotic nature of the partial differential equations used to calculate the forecast—introduce errors that double every five days [28-29]. The use of model ensemble forecasts since the 1990s helps to define the forecast uncertainty and extend weather forecasting further into the future than otherwise possible [30-32].

2.4 Initialization

The atmosphere is a fluid. As such, the idea of numerical weather prediction is to sample the state of the fluid at a given time and use the equations of fluid dynamics and thermodynamics to estimate the state of the fluid at some time in the future. On land, terrain maps, available at resolutions down to 1 kilometre globally, are used to help model atmospheric circulations within regions of rugged topography, in order to better depict features such as downslope winds, mountain waves, and related cloudiness which affects incoming solar radiation [33]. The main inputs from country-based weather services are surface observations from automated weather stations at ground level over land and from weather buoys at sea. The World Meteorological Organization acts to standardize the instrumentation, observing practices and timing of these observations worldwide. Stations either report hourly in METAR reports [34], or every six hours in SYNOP reports [35]. Models are initialized using this observed data. The irregularly spaced observations are processed by data assimilation and objective analysis methods, which perform quality control and obtain values at locations usable by the model's mathematical algorithms. The grid used for global models is geodesic or icosahedral, spaced by latitude, longitude, and elevation [36]. The data are then used in the model as the starting point for a forecast [37].

A variety of methods are used to gather observational data for use in numerical models. Sites launch radiosondes, which rise through the troposphere and well into the stratosphere [38]. Information from weather satellites is used where traditional data sources are not available. Commerce provides pilot reports along aircraft routes [39] and ship reports along shipping routes [40]. Research projects use reconnaissance aircraft to fly in and around weather systems of interest, such as tropical cyclones [41-42]. Reconnaissance aircraft are also flown over the open oceans during the cold season into systems that cause significant uncertainty in forecast guidance, or are expected to be of high impact 3–7 days into the future over the downstream continent [43]. Sea ice began to be initialized in forecast models in 1971 [44]. Efforts to involve sea surface temperature in model initialization began in 1972 due to its role in modulating weather in higher latitudes of the Pacific [45].

2.5 Parameterization

Weather and climate model gridboxes have sides of between 5 kilometres and 300 kilometres. A typical cumulus cloud has a scale of less than 1 kilometre, and would require a grid even finer than this to be represented physically by the equations of fluid motion. Therefore, the processes that such clouds represent are parameterized, by processes of various sophistication. In the earliest models, if a column of air in a model gridbox was unstable (i.e., the bottom warmer than the top) then it would be overturned, and the air in that vertical column mixed. More sophisticated schemes add enhancements, recognizing that only some portions of the box might convect and that entrainment and other processes occur. Weather models that have gridboxes with sides between 5 kilometres and 25 kilometres can explicitly represent convective clouds, although they still need to parameterize cloud microphysics [46]. The formation of large-scale (stratus-type) clouds is more physically based, they form when the relative humidity reaches some prescribed value. Still, sub grid scale

processes need to be taken into account. Rather than assuming that clouds form at 100% relative humidity, the cloud fraction can be related to a critical relative humidity of 70% for stratus-type clouds, and at or above 80% for cumuliform clouds [47], reflecting the sub grid scale variation that would occur in the real world.

The amount of solar radiation reaching ground level in rugged terrain, or due to variable cloudiness, is parameterized as this process occurs on the molecular scale [48]. Also, the grid size of the models is large when compared to the actual size and roughness of clouds and topography. Sun angle as well as the impact of multiple cloud layers is taken into account [49]. Soil type, vegetation type, and soil moisture all determine how much radiation goes into warming and how much moisture is drawn up into the adjacent atmosphere. Thus, they are important to parameterize [50].

2.6 Domains

The horizontal domain of a model is either global, covering the entire Earth, or regional, covering only part of the Earth. Regional models also are known as limited-area models, or LAMs. Regional models use finer grid spacing to resolve explicitly smaller-scale meteorological phenomena, since their smaller domain decreases computational demands. Regional models use a compatible global model for initial conditions of the edge of their domain. Uncertainty and errors within LAMs are introduced by the global model used for the boundary conditions of the edge of the regional model, as well as within the creation of the boundary conditions for the LAMs itself [51].

The vertical coordinate is handled in various ways. Some models, such as Richardson's 1922 model, use geometric height (z) as the vertical coordinate. Later models substituted the geometric z coordinate with a pressure coordinate system, in which the geopotential heights of constant-pressure surfaces become dependent variables, greatly simplifying the primitive equations [52]. This follows since pressure decreases with height through the Earth's atmosphere [53]. The first model used for operational forecasts, the single-layer barotropic model, used a single pressure coordinate at the 500-millibar (15 inHg) level [15], and thus was essentially two-dimensional. High-resolution models—also called mesoscale models—such as the Weather Research and Forecasting model tend to use normalized pressure coordinates referred to as sigma coordinates [54].

2.6.1 Global versions

Some of the better known global numerical models are:

- GFS Global Forecast System (previously AVN) – developed by NOAA,
- NOGAPS – developed by the US Navy to compare with the GFS,
- GEM Global Environmental Multiscale Model – developed by the Meteorological Service of Canada (MSC),
- IFS developed by the European Centre for Medium-Range Weather Forecasts,
- UM Unified Model developed by the UK Met Office,

- ICON developed by the German Weather Service, DWD, jointly with the Max-Planck-Institute (MPI) for Meteorology, Hamburg, NWP Global model of DWD,
- ARPEGE developed by the French Weather Service, Météo-France,
- IGCM Intermediate General Circulation Model [5].

2.6.2 Regional versions

Some of the better known regional numerical models are:

- **WRF** The Weather Research and Forecasting model was developed cooperatively by NCEP, NCAR, and the meteorological research community. WRF has several configurations, including:
    - **WRF-NMM** The WRF Nonhydrostatic Mesoscale Model is the primary short-term weather forecast model for the U.S., replacing the Eta model,
    - **WRF-ARW** Advanced Research WRF developed primarily at the U.S. National Center for Atmospheric Research (NCAR).
- **NAM** The term North American Mesoscale model refers to whatever regional model NCEP operates over the North American domain. NCEP began using this designation system in January 2005. Between January 2005 and May 2006, the Eta model used this designation. Beginning in May 2006, NCEP began to use the WRF-NMM as the operational NAM,
- **RAMS** the Regional Atmospheric Modelling System developed at Colorado State University for numerical simulations of atmospheric meteorology and other environmental phenomena on scales from meters to hundreds of kilometers – now supported in the public domain,
- **MM5** The Fifth Generation Penn State/NCAR Mesoscale Model,
- **ARPS** the Advanced Region Prediction System developed at the University of Oklahoma is a comprehensive multi-scale nonhydrostatic simulation and prediction system that can be used for regional-scale weather prediction up to the tornado-scale simulation and prediction. Advanced radar data assimilation for thunderstorm prediction is a key part of the system,
- **HIRLAM** High Resolution Limited Area Model, is developed by the European NWP research consortia HIRLAM co-funded by 10 European weather services. The meso-scale HIRLAM model is known as HARMONIE and developed in collaboration with Météo-France and ALADIN consortia,
- **GEM-LAM** Global Environmental Multiscale Limited Area Model, the high resolution 2.5 km GEM by the Meteorological Service of Canada (MSC),
- **ALADIN** The high-resolution limited-area hydrostatic and non-hydrostatic model developed and operated by several European and North African countries under the leadership of Météo-France [5],
- **COSMO** The COSMO Model, formerly known as LM, aLMo or LAMI, is a limited-area non-hydrostatic model developed within the framework of the Consortium for Small-Scale Modelling (Germany, Switzerland, Italy, Greece, Poland, Romania, and Russia) [55],

- **Meso-NH** The Meso-NH Model [56] is a limited-area non-hydrostatic model developed jointly by the Centre National de Recherches Météorologiques and the Laboratoire d'Aérologie (France, Toulouse) since 1998 [57]. Its application is from mesoscale to centimetric scales weather simulations.

2.7 Model output statistics

Because forecast models based upon the equations for atmospheric dynamics do not perfectly determine weather conditions near the ground, statistical corrections were developed to attempt to resolve this problem. Statistical models were created based upon the three-dimensional fields produced by numerical weather models, surface observations, and the climatological conditions for specific locations. These statistical models are collectively referred to as model output statistics (MOS) [58], and were developed by the National Weather Service for their suite of weather forecasting models [26]. The United States Air Force developed its own set of MOS based upon their dynamical weather model by 1983 [27].

Model output statistics differ from the perfect prog technique, which assumes that the output of numerical weather prediction guidance is perfect [59]. MOS can correct for local effects that cannot be resolved by the model due to insufficient grid resolution, as well as model biases. Forecast parameters within MOS include maximum and minimum temperatures, percentage chance of rain within a several hour period, precipitation amount expected, chance that the precipitation will be frozen in nature, chance for thunderstorms, cloudiness, and surface winds [60].

2.8 Applications

2.8.1 Climate modelling

In 1956, Norman Phillips developed a mathematical model that realistically depicted monthly and seasonal patterns in the troposphere. This was the first successful climate model [22-23]. Several groups then began working to create general circulation models [61]. The first general circulation climate model combined oceanic and atmospheric processes and was developed in the late 1960s at the Geophysical Fluid Dynamics Laboratory, a component of the U.S. National Oceanic and Atmospheric Administration [62]. By the early 1980s, the U.S. National Center for Atmospheric Research had developed the Community Atmosphere Model (CAM), which can be run by itself or as the atmospheric component of the Community Climate System Model. The latest update (version 3.1) of the standalone CAM was issued on 1 February 2006 [63-65]. In 1986, efforts began to initialize and model soil and vegetation types, resulting in more realistic forecasts [66]. Coupled ocean-atmosphere climate models, such as the Hadley Centre for Climate Prediction and Research's HadCM3 model, are being used as inputs for climate change studies [61].

2.8.2 Limited area modelling

Air pollution forecasts depend on atmospheric models to provide fluid flow information for tracking the movement of pollutants [67]. In 1970, a private company in the U.S. developed the regional Urban Airshed Model (UAM), which was used to forecast the effects of air pollution and acid rain. In the mid- to late-1970s, the United

States Environmental Protection Agency took over the development of the UAM and then used the results from a regional air pollution study to improve it. Although the UAM was developed for California, it was during the 1980s used elsewhere in North America, Europe, and Asia [25].

The Movable Fine-Mesh model, which began operating in 1978, was the first tropical cyclone forecast model to be based on atmospheric dynamics [24]. Despite the constantly improving dynamical model guidance made possible by increasing computational power, it was not until the 1980s that numerical weather prediction (NWP) showed skill in forecasting the track of tropical cyclones. And it was not until the 1990s that NWP consistently outperformed statistical or simple dynamical models [68]. Predicting the intensity of tropical cyclones using NWP has also been challenging. As of 2009, dynamical guidance remained less skillful than statistical methods [69].

2.9 The atmospheric model PALM

The previous information was very general concerning atmospheric models. For the needs of the Working Package 3 of the HYPERION project the atmospheric model PALM was used. This section gives details about the model.

2.9.1 General

The model PALM is based on the non-hydrostatic, filtered, incompressible Navier-Stokes equations in Boussinesq-approximated form (an anelastic approximation is available as an option for simulating deep convection). By default, PALM has at least six prognostic quantities: the velocity components u, v, w on a Cartesian grid, the potential temperature θ, water vapor mixing ratio q_v and possibly a passive scalar s. Furthermore, an additional equation is solved for either the subgrid-scale turbulent kinetic energy (SGS-TKE) e (LES mode, default) or the total turbulent kinetic energy (RANS mode).

In the LES mode, the filtering process yields four subgrid-scale (SGS) covariance terms. These SGS terms are parametrized using a 1.5-order closure after Deardorff (1980). PALM uses the modified version of Moeng and Wyngaard (1988) and Saiki et al. (2000). The closure is based on the assumption that the energy transport by SGS eddies is proportional to the local gradients of the mean quantities.

The following sections outline the most important specifics of PALM. For a more detailed description, and the references given in this section, can be found in PALM documentation (https://palm.muk.uni-hannover.de/trac/wiki/doc) and related publications (Raasch and Schröter, 2001; Maronga et al., 2015).

2.9.2 Discretization in time and space

The model domain in PALM is discretized in space using finite differences and equidistant horizontal grid spacings. The Arakawa staggered C-grid (Harlow and Welch, 1965; Arakawa and Lamb, 1977) is used, where scalar quantities are defined at the center of each grid volume, whereas velocity components are shifted by half a grid width in their respective direction so that they are defined at the edges of the grid volumes. By default, the advection terms in the prognostic equations are discretized using an upwind-biased 5th-order differencing scheme (Wicker and Skamarock, 2002)

in combination with a 3rd-order Runge–Kutta time-stepping scheme after Williamson (1980).

2.9.3 Pressure solver

The Boussinesq approximation requires incompressibility of the flow, but the integration of the governing equations does not provide this feature. Divergence of the flow field is thus inherently produced. Hence, a predictor corrector method is used where an equation is solved for the modified perturbation pressure after every time step (e.g., Patrinos and Kistler, 1977). In case of cyclic lateral boundary conditions, the solution of the Poisson equation is achieved by using a direct fast Fourier transform (FFT). PALM provides the inefficient but less restrictive Singleton-FFT (Singleton, 1969) and the well optimized Temperton-FFT (Temperton, 1992). External FFT libraries can be used as well, with the FFTW (Frigo and Johnson, 1998) being the most efficient one. Alternatively, the iterative multigrid scheme can be used (e.g., Hackbusch, 1985). This scheme uses the Gauss–Seidel method for the inner iterations on each grid level.

2.9.4 Boundary conditions

PALM offers a variety of boundary conditions. Dirichlet or Neumann boundary conditions can be chosen for u, v, θ, q_v, and p^* at the bottom and top of the model. For the horizontal velocity components, the choice of Neumann (Dirichlet) boundary conditions yields free-slip (no-slip) conditions. Neumann boundary conditions are also used for the SGS-TKE. Kinematic fluxes of heat and moisture can be prescribed at the surface instead (Neumann conditions) of temperature and humidity (Dirichlet conditions). At the top of the model, Dirichlet boundary conditions can be used with given values of the geostrophic wind. Vertical velocity is assumed to be zero at the surface and top boundaries, which implies using Neumann conditions for pressure.

Following Monin-Obukhov similarity theory (MOST) a constant flux layer can be assumed as boundary condition between the surface and the first grid level where scalars and horizontal velocities are defined. In PALM it is assumed that MOST can be also applied locally and therefore local fluxes, velocities, and scaling parameters are calculated. This scheme involves calculation of the Obukhov length L, which can be either done based on variables of the previous time step ("circular"), via a Newton iteration method, or via a look-up table for the stability parameter z/L.

2.9.5 Topography parameterization

The Cartesian topography (complex terrain and buildings) in PALM is generally based on the mask method (Briscolini and Santangelo, 1989) and allows for explicitly resolving solid obstacles such as buildings and orography. The implementation makes use of the following simplifications:

1. the obstacle shape is approximated by (an appropriate number of) full grid cells to fit the grid, i.e., a grid cell is either 100% fluid or 100% obstacle,
2. the obstacles are fixed (not moving).

Topography is realized in 3-D, e.g., overhanging structures as for example bridges, ceilings, or tunnels, are allowed, i.e., topography does not necessarily be surface-mounted. If no overhanging structures are present, the 3-D obstacle dimension

reduces to a 2.5-D topography format, which conforms to the Digital Elevation Model (DEM) format (DEMs of city morphologies have become increasingly available worldwide due to advances in remote sensing technologies). In case of overhanging structures, however, 3-D topography information is required to mask obstacles and their faces in PALM.

The model domain is then separated into three subdomains:

A. grid points in free fluid without adjacent surfaces, where the standard PALM code is executed,
B. grid points next to surface that require extra code (e.g., surface parametrization), and
C. grid points within obstacles, where the standard PALM code is executed but multiplied by zero.

Additional topography code is executed in grid volumes of subdomain B. The faces of the obstacles are always located where the respective surface-normal velocity components u, v, and w are defined so that the impermeability boundary condition can be implemented by setting the respective surface-normal velocity component to zero.

In case of 5th-order advection scheme, the numerical stencil at grid points adjacent to obstacles would require data which is located within the obstacle. In order to avoid this, the order of the advection scheme is successively degraded at respective grid volumes adjacent to obstacles, i.e., from the 5th-order to 3rd-order at the second grid point above/beside an obstacle and from 3rd-order to 1st-order at grid points directly adjacent to an obstacle.

Simulations with topography require the application of MOST between each surface and the first computational grid point outside of the topography. For vertical and horizontal downward-facing surfaces, neutral stratification is assumed for MOST.

Buildings are primarily realized as obstacles that react to the flow dynamics via form drag and friction forces by assuming a constant flux layer between the building surface and the adjacent air volume. A simple thermodynamic coupling is also possible by prescribing surface fluxes of sensible (and latent heat) at any of the building surface grid elements. Thermodynamic interactive buildings are realized within the PALM-4U (https://palm.muk.uni-hannover.de/trac/wiki/palm4u) components.

The technical realization of the topography and treatment of surface-bounded grid cells are outlined in Section “Topography implementation” of the online PALM documentation (https://palm.muk.uni-hannover.de/trac/wiki/doc/tec/topography).

2.9.6 Parallelization and scaling

The parallelization of the code is achieved by a 2-D domain decomposition method along the x and y direction with equally sized subdomains. Ghost layers are added at the side boundaries of the subdomains in order to account for the local data dependencies, which are caused by the need to compute finite differences at these positions. The number of ghost layers that are used in PALM depend on the order of the advection scheme, with three layers for the 5th-order Wicker-Skamarock scheme.

Ghost layer data are exchanged after every time step. Data exchange between processor cores is realized using the Message Passing Interface (MPI). Additional loop vectorization via OpenMP is realized which also allows a so-called hybrid parallelization.

PALM shows excellent scaling which was tested for up to 50,000 processor cores (https://palm.muk.uni-hannover.de/trac/wiki/doc/tec/parallel#Parallelizationandoptimizationdetails).

2.9.7 External forcing and nesting

Usually, PALM is used to simulate the flow in the boundary layer which is a certain part of the atmosphere. Processes occurring on larger scales than those in the boundary layer including large scale advection of scalars, large scale pressure gradients or large-scale subsidence have also to be considered in the model, especially when focusing on realistic situations observed during measurement campaigns. In limited domain models with non-cyclic boundary conditions the large-scale state enters through the boundary conditions at the lateral walls, and is usually taken from larger-scale models. An additional possibility to account for tendencies in the LES model resulting from larger scales than those in the boundary layer is the usage of nudging. Nudging is a (Newtonian) relaxation technique which adjusts the large-eddy simulation to a given, larger scale flow situation (Anthes, 1974; Stauffer and Bao, 1993). Alternatively, a nesting system is available which allows for self-nesting of PALM, i.e., running a parent domain run at coarse grid resolution and large model domain with a nested child model domain run at finer resolution and smaller domain.

2.9.8 Ocean option and coupling to atmosphere

PALM allows for studying the ocean mixed layer (OML) by using an ocean option where the sea surface is defined at the top of the model, so that negative values of z indicate the depth.

A coupled mode for the atmospheric and oceanic versions of PALM has been developed in order to allow for studying the interaction between turbulent processes in the ABL and OML. The coupling is realized by the online exchange of information at the sea surface (boundary conditions) between two PALM runs (one atmosphere and one ocean). The atmospheric model uses a constant flux layer and transfers the kinematic surface fluxes of heat and moisture as well as the momentum fluxes to the oceanic model. Flux conservation between the ocean and the atmosphere requires an adjustment of the fluxes for the density of water.

2.9.9 Embedded models

PALM comes with an increasing number of embedded models:

- Cloud microphysics,
- Lagrangian particle model (LPM),
- Lagrangian cloud model (LCM),
- Canopy model,
- 1D model for precursor runs,
- Land surface model,

- Radiation models,
- Wind turbine model.

For more details, see PALM documentation (https://palm.muk.uni-hannover.de/trac/wiki/doc).

2.9.10 Data output and handling

Due to the enormous amount of data that comes along with computationally expensive LES, the data handling plays a key role for the performance of LES models and for data analysis during post-processing. PALM is optimized to pursue the strategy of performing data operations to great extent online during the simulation instead of postpone these operations to the post-processing. In this way, the data output (e.g., of huge 4-D data, or temporal averages) can be significantly reduced. In order to allow the user to perform own calculations during runtime, the user interface offers a wide range of possibilities, e.g., for defining user-defined output quantities.

PALM allows data output for different quantities as time series, (horizontally-averaged) vertical profiles, 2-D cross sections, 3-D volume data, and masked data. All data output files are in netCDF format, which can be processed by different public domain and commercial software. NetCDF data can also be easily read from Fortran programs, provided that a netCDF library is available. The netCDF libraries currently support three different binary formats for netCDF files: classic, 64-bit offset, and netCDF-4. The latter was introduced in netCDF version 4.0 and is based on the HDF5 (http://www.hdfgroup.org/HDF5) data format. PALM is able to handle all three netCDF formats and also supports parallel I/O for netCDF-4.

2.9.11 The use of PALM in the HYPERION project

In Working Package 3 of the HYPERION project, a combination of data analysis methods, on the basis of existing data sets, as well as two way coupled multi-scale numerical modelling systems and techniques has been utilized using PALM. This work was performed by FMI and AUTH and is described in detail in Deliverable “D3.3.1 Report on dynamical downscaling of wind forecast system and first downscaling simulation results”.

3. Seismic models

3.1. Seismic Hazard Analysis Framework

The earthquake hazard can be typically quantified following either scenario-based or probabilistic seismic hazard analysis (SHA). The main difference between those approaches is how they treat uncertainty related to the probability of occurrence of future earthquakes in terms of time, space and magnitude. In Scenario-based SHA (SSHA) the earthquake characteristics e.g., magnitude, distance etc. are assumed to be deterministic, and representative of specific scenarios; thus the respective uncertainties are neglected. SSHA is straightforward and simple to implement and typically is performed for the worst-case scenario that threatens most the site of interest. On the contrary, Probabilistic SHA (PSHA, [70]) allows accounting for uncertainties related to the earthquake’s occurrence at the cost of being

computationally more expensive that SSHA, as it accounts for all potential earthquake sources in an area when computing the seismic hazard. In HYPERION the seismic hazard is assessed following the principles of PSHA, under three approaches: Classical PSHA, Event-Based Seismic Hazard Analysis and Disaggregation analysis ([71, 72]). Classical PSHA offers a "timeless" (or time-of-occurrence-agnostic) assessment of the seismic hazard allowing to perform comparative hazard assessment at different locations. On the contrary, event-based analysis simulates on an event-basis the seismicity of a region in a given time-span as described by the source model. Event-based PSHA provides spatially correlated information of the seismic hazard, thus is better suited for risk and resilience assessment of spatially distributed interconnected assets that are vulnerable to the seismic hazard. Seismic hazard Disaggregation analysis is an extension of classical PSHA and allows identifying the extent to which different earthquake sources, magnitudes etc. contribute to the seismic hazard.

3.1.1 Classical Probabilistic Seismic Hazard Analysis

Classical PSHA aims to quantify the Mean Annual Frequency (MAF) of exceeding any level of the shaking intensity, as described by the Intensity Measure (IM, see [73]). It accounts for the inherent uncertainties in the seismic occurrence, such as those related to the rupture's location, earthquake's size, occurrence rate etc. Classical PSHA can be summarized in the following five steps, that are schematically presented in Figure 1:

1. All earthquake sources able to produce ground motions of engineering importance at the site of interest are identified. Typically, two types of earthquake sources are included in the analysis: faults and areas. The former is used to model seismicity on identified faults, whose characteristics can be determined based on past observations. On the contrary, areas are adopted to model distributed seismicity, i.e., to account for the possibility that earthquakes may occur anywhere within the area. The most comprehensive seismic source models used in PSHA account for both seismicity on faults and distributed seismicity.
2. For each seismic source the distribution of earthquake magnitudes is identified. This describes the annual occurrence rate of earthquakes greater or equal than magnitude m. An example is presented in Figure 1(b) for a distribution following the bounded Gutenberg-Richter recurrence law. This sets an upper limit on the earthquake magnitude to account for the physical constrains imposed by the finite fault size.
3. For each seismic source the distribution of source-to-site distance is identified, as presented in Figure 1(c). Since the seismic sources have been determined in step 1, the distance distribution can be calculated geometrically assuming that earthquakes are expected to occur anywhere within the source (area or fault) with an equal probability.

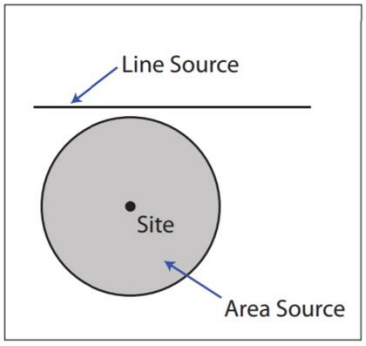

(a) earthquake sources

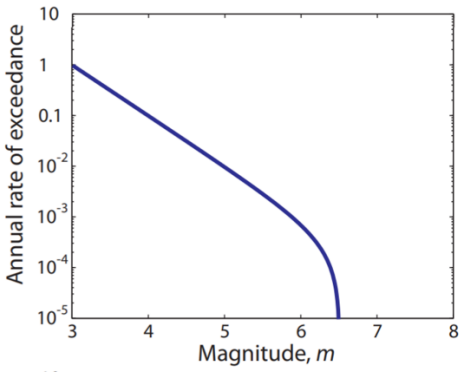

(b) source's distribution of earthquake magnitude

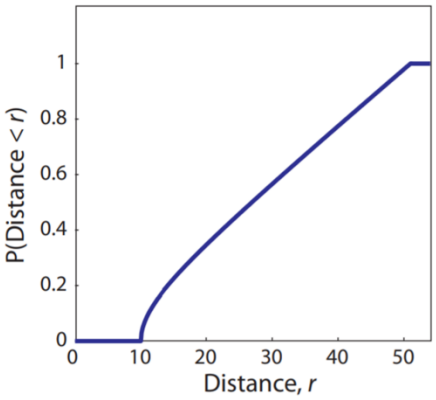

(c) source-to-site distance distribution

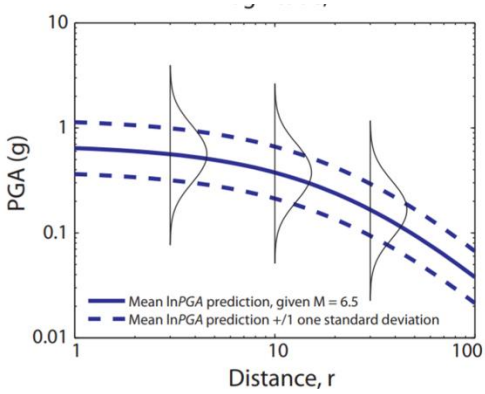

(d) distribution of the ground motion intensity

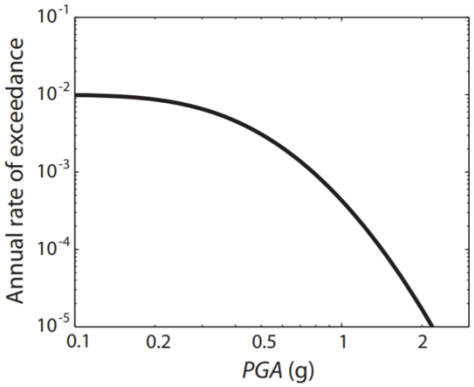

(e) annual rate of exceeding the ground motion intensity

Figure 1: PSHA steps (adapted from [74]).

4. The distribution of ground motion intensity is determined as a function of the earthquake's variables such as magnitude, distance, epsilon etc. The functions that describe this distribution are the so-called called ground motion prediction equations (GMPEs). They are typically generated via regression analysis in past earthquake observations. GMPEs provide the statistical distribution of the ground motion intensity rather than single deterministic values, which allow predictive models to predict extremes rather than only the

mean values. An example is presented in Figure 1(d), where the fitted distribution is represented by its mean (continuous line) and standard deviation (dashed line) of the natural logarithm of the data.

5. Information from steps 1-4 is combined through the total probability theorem to compute the MAF of IM exceeding ground motion intensity x as:

$$\lambda(IM > x) = \sum_{i=1}^{N_{srcs}} v_i \int_{M_{\min}}^{M_{\max,i}} \int_{0}^{R_{\max,i}} \mathrm{P}(IM > x \mid M, R, site)\, f_i(M, R)\, \mathrm{d}M\, \mathrm{d}R \qquad (4)$$

where N_{srcs} are the number of earthquake sources, M is the earthquake magnitude, R is the distance, P($IM>x|M,R,site$) is the probability of IM exceeding x given the occurrence of an earthquake with magnitude m at distance R, $f_i(M, R)$ is the joint magnitude-distance probability density function of the i^{th} source, $M_{max,i}$ is the maximum magnitude of the i^{th} source and v_i is the annual frequency of events with $m>M_{min}$ generated by the i^{th} source. The function of $\lambda(IM>x)$ is the so-called seismic hazard curve that is schematically presented in Figure 1(e) and provides the MAF of exceeding the IM.

3.1.2 Event-Based Seismic Hazard Analysis

Event-based seismic hazard analysis can be employed to compute stochastic event sets (SES) for a given area of interest, each of them representing a possible realization of the seismicity occurring in a given time-span, as described by the source model. SES are synthetic catalogues of earthquake ruptures for which the shaking intensity is defined by accounting for the uncertainties implied by the ground motion prediction equations prescribed in the source model. For each rupture in the SES a number of alternative ground motion fields are derived, that represent different realizations of the spatially distributed IM values caused by the given rupture. An example of an SES is presented in Figure 2 for a period of 10,000 years, where the circles indicate the location of the rupture and the color indicates the earthquake's magnitude. An example of a ground motion field is presented in Figure 3 for Peak Ground Acceleration (PGA), showing spatially correlated values of the seismic intensity over the area of interest.

In contrast to classical PSHA that provides a timeless assessment of the seismic hazard, event-based analysis discretises the hazard in events and allows the estimation of simultaneous damages in multiple spatially distributed assets. This makes event-based analysis the go-to option for seismic risk and resilience assessment especially in cases of interconnected systems as for a water supply system or a transportation network. Although classical and event-based analysis seem to be different, in reality they are linked to each other since the seismic-events generated by the latter should be able to reproduce the time-averaged values of the former. This requires that the effective time-span of event-based analysis is large enough, i.e., a large number of SES is modelled for a large time-span.

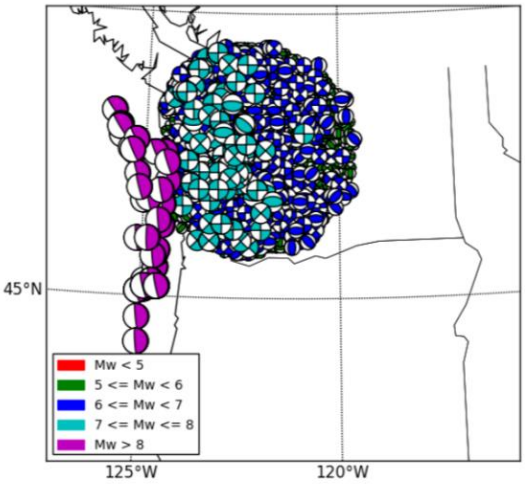

Figure 2: Stochastic event set for a duration of 10,000 years. The colors represent the rupture's magnitude while the location of the circles is indicative of the rupture's position (adopted from [75]).

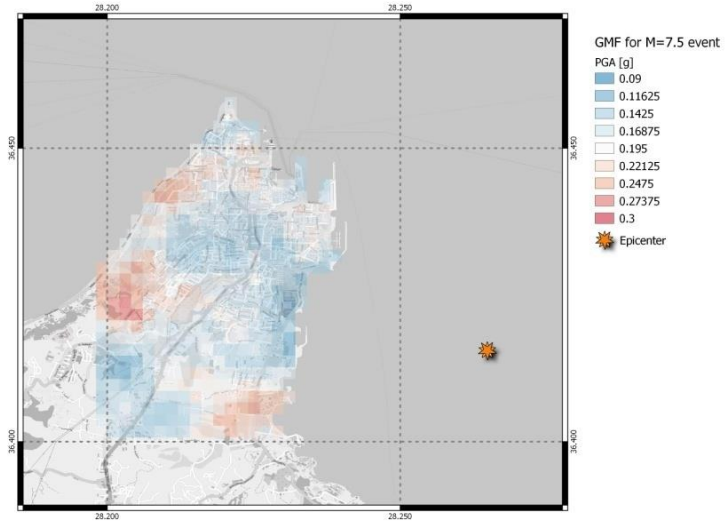

Figure 3: Ground motion field showing spatially correlated values of the seismic intensity.

3.1.3 Seismic Hazard Disaggregation Analysis

Classical PSHA aggregates all seismic scenarios when computing the seismic hazard, thus identifying which one is most likely to cause exceedance of a given ground motion intensity is not straightforward. For this reason, seismic hazard disaggregation analysis is performed to identify how different earthquake sources and magnitudes contribute to the rate of exceedance of a given ground motion intensity at a site. Disaggregation is typically performed in terms of magnitude, source-to-site distance and often epsilon, that is a measure of the deviation of mean to the predicted value of the ground motion prediction equation. An example of disaggregation analysis results is

presented in Figure 4, where the contribution of different magnitude-distance combinations to the seismic hazard is presented by the bins. Disaggregation analysis results can also be used to select a number of ground motion records that are consistent to the site-specific seismic hazard. The site-specific hazard-compatible ground motion records act as a link between seismic hazard analysis and probabilistic seismic demand analysis of structures. One of the most comprehensive methods for record selection relies upon the Conditional Spectrum ([76, 77]) that is determined for the mean disaggregation scenario and is used as a basis to select the ground motion records.

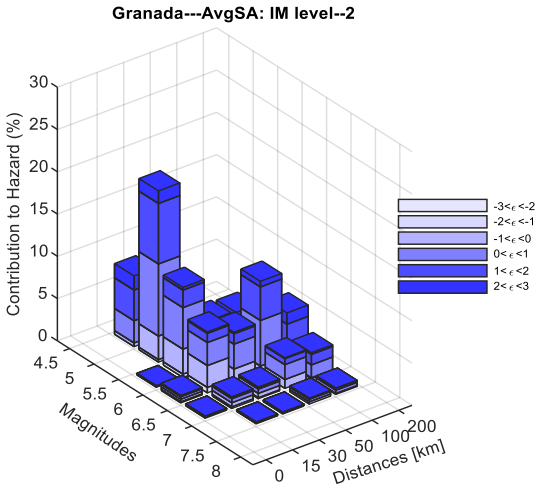

Figure 4: Seismic hazard disaggregation results showing the contribution of each combination of magnitude, M_w, and rupture distance, R_{Rup}, to the seismic hazard for the city of Granada.

3.2 Seismic hazard assessment for the HYPERION demo sites

The seismic hazard is assessed via the open-source OpenQuake platform [79] for Rhodes, Granada and Venice, while Tonsberg is not in a seismically active region. The area source model [80-82] of the SHARE project is employed for the analysis (Figure 5) along with the ground motion prediction equation proposed by [83]. The state-of-the-art average spectral acceleration, *AvgSa*, [84-86] is adopted as the IM:

$$AvgSa(T_{Ri}) = \left(\prod_{i=1}^{n} Sa(T_{Ri}) \right)^{1/n} \quad (5)$$

It is estimated by combining n spectral acceleration ordinates, Sa, at periods T_{Ri}. Each ordinate is the geometric mean of the 5%-damped spectral acceleration from the two horizontal components. Herein, the period range of $[0.2, 2.0]$s with an increment of 0.1 sec is adopted. The Peak Ground Acceleration, *PGA*, as well as the Peak Ground Velocity, *PGV*, are also adopted as additional IMs.

Figure 5: Area source model of the SHARE project adopted for seismic hazard analysis of the Greek demo site.

3.2.1 Classical PSHA analysis results

Classical PSHA is performed for the 3 seismically active regions to compute the seismic hazard curves. The results for Rhodes and Granada are presented in Figures 6 and 7, respectively, in terms of *AvgSa.* Characteristic values of *AvgSa* corresponding to 2%, 10% and 30% probability of exceedance, *P*, in $T = 50$ years, or equivalently to $MAF = -\ln(1-P) / T$=0.0004, 0.0021 and 0.0044, are summarized in Tables 2 and 3 for the two sites.

Table 1. *IM* value, mean magnitude, distance and epsilon for Rhodes.

IM Level	% in 50 years	Rhodes			
		AvgSA **[g]**	$\bar{M}$	$\bar{R}$ **[km]**	$\bar{\varepsilon}$
1	70	0.087	6.59	80.26	1.08
2	50	0.113	6.70	77.00	1.13
3	30	0.154	6.82	73.78	1.19
4	10	**0.256**	7.05	69.84	1.35
5	5	0.334	7.17	68.53	1.47
6	2	0.456	7.30	67.60	1.67
7	1.5	0.498	7.34	67.46	1.73
8	1	0.561	7.39	67.32	1.82
9	0.6	0.644	7.44	67.26	1.93
10	0.2	0.839	7.55	67.45	2.17

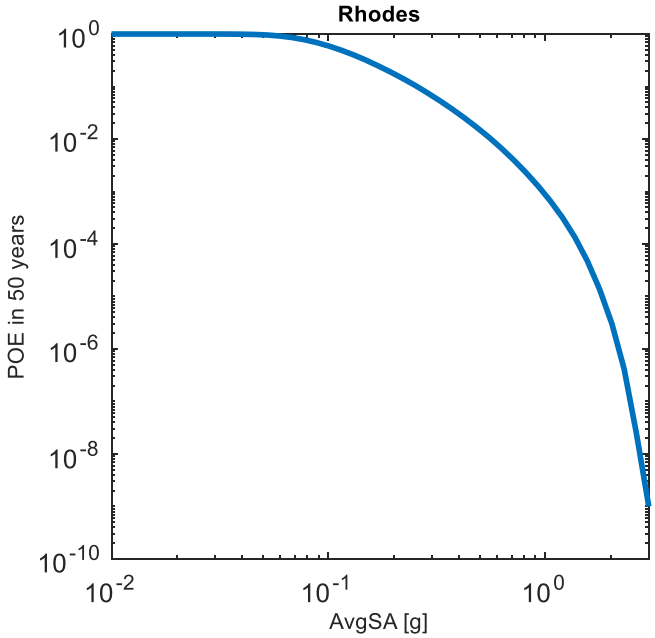

Figure 6: Seismic hazard curve computed for Rhodes, Greece in terms of average spectral acceleration, *AvgSa*. The hazard curve is obtained using the area source model of the SHARE project and the BA08 [83] GMPE.

Table 3. *IM* value, mean magnitude, distance and epsilon for Rhodes.

IM Level	% in 50 years	Granada			
		AvgSA **[g]**	$\bar{M}$	$\bar{R}$ **[km]**	$\bar{\varepsilon}$
1	70	0.026	5.73	52.3	0.81
2	50	0.037	5.82	45.8	0.88
3	30	0.054	5.92	38.2	0.95
4	10	**0.104**	6.08	26.4	1.06
5	5	0.148	6.17	20.9	1.10
6	2	0.230	6.29	15.7	1.16
7	1.5	0.262	6.33	14.4	1.19
8	1	0.313	6.38	13.0	1.23
9	0.6	0.387	6.44	11.7	1.30
10	0.2	0.587	6.57	10.0	1.50

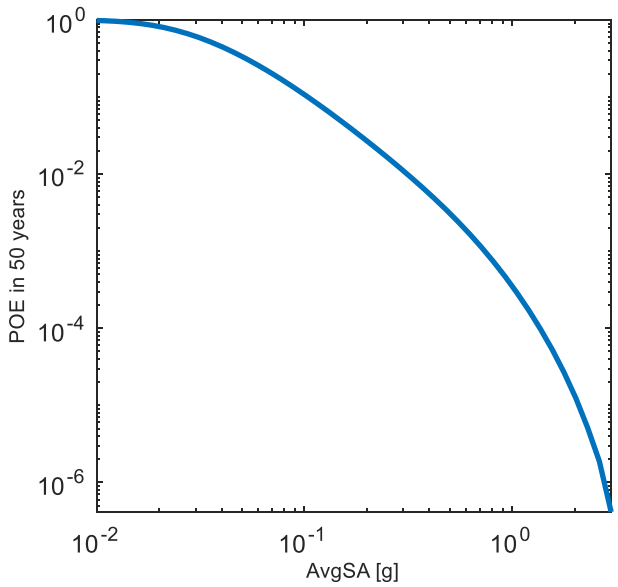

Figure 7: Seismic hazard curve computed for Granada, Spain in terms of average spectral acceleration, *AvgSa*. The hazard curve is obtained using the area source model of the SHARE project and the BA08 [83] GMPE.

3.2.2 Event-based seismic hazard analysis results

Event-based seismic hazard analysis is performed for Rhodes, Granada and Venice to identify SES as well as the ground motion fields for the ruptures belonging to them. An example of three ground motion fields is presented in Figure 8.

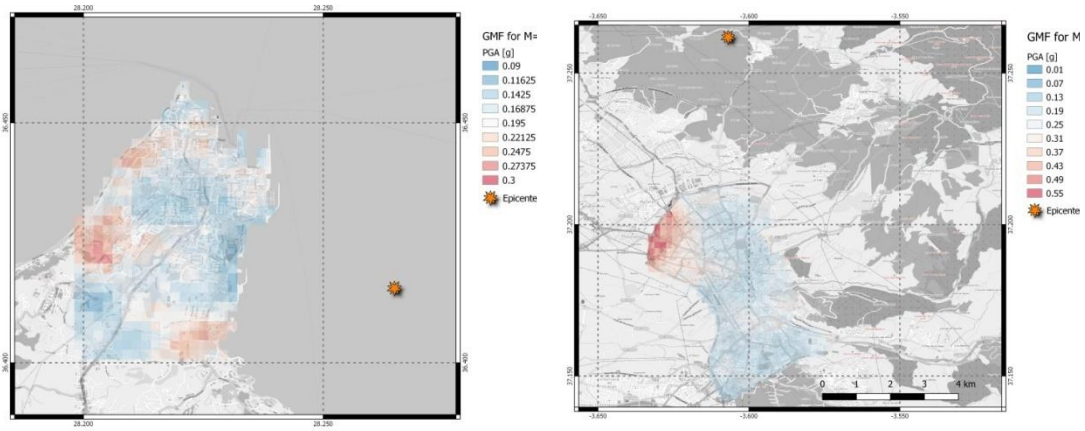

a) Rhodes GMF M7.5 b) Granada GMF M7.1

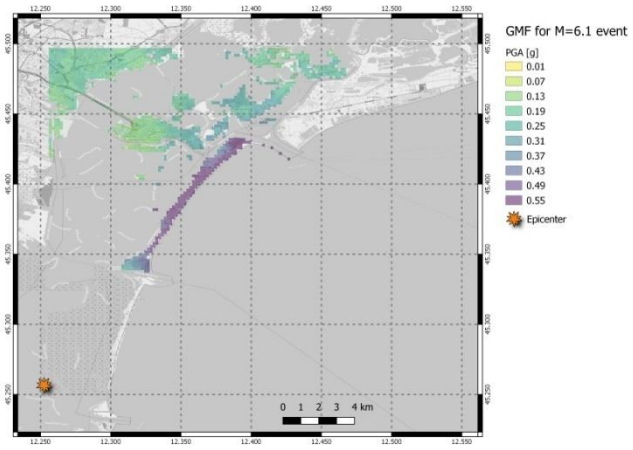

c) Venice GMF M6.1

Figure 8: Example of three PGA ground motion fields derived for a) Rhodes, b) Granada and c) Venice.

3.2.3 Disaggregation analysis results and record selection

Seismic hazard disaggregation is performed for the demo sites. The results for Granada and Rhodes are presented, at three hazard levels i.e., those with probability of exceedance 30%, 10% and 2% in 50years, henceforth mentioned as 30%/50yr, 10%/50yr and 2%/50yr, respectively. The results are presented in Figures 9-14 for Rhodes and Figures 15-20 for Granada, for each of the three hazard levels.

Specifically for Rhodes, disaggregation analysis results appear in Figures 10, 12, and 14 at the 30%/50yr, 10%/50yr and 2%/50yr levels, respectively. Based on these results, a set of 21 records is selected that are compatible with the Conditional Spectrum determined for the mean disaggregation scenario. The Conditional Spectrum as well as the response spectra of the 21 selected records for Rhodes are shown in Figures 9, 11, and 13, while the selected sets of ground motions per the NGA-West database [87] appear in Tables 4 – 6 along with the appropriate scaling factors by which they need to be scaled to match the respective hazard level.

Similarly for Granada, Figures 16, 18, and 20 show the disaggregation analysis results at the 30%/50yr, 10%/50yr and 2%/50yr levels, respectively. The Conditional Spectra as well as the matching of the 21 compatible records per hazard level for Granada are shown in Figures 15, 17 and 19. The selected ground motions per hazard level, appear in Tables 7 – 9 along with the appropriate scaling factors needed to match the respective hazard level.

Rhodes

Hazard level: 30%/50yr

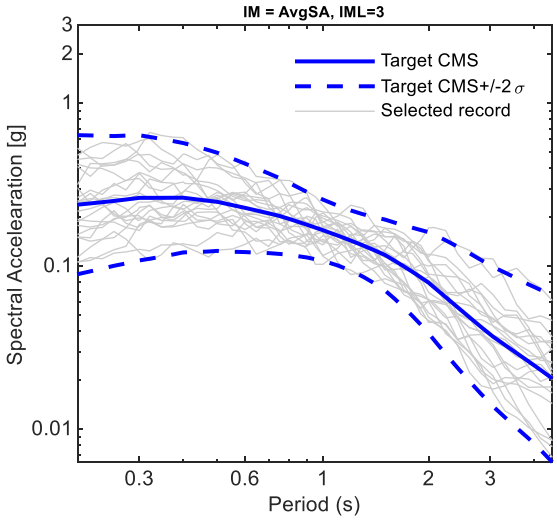

(a) response spectra

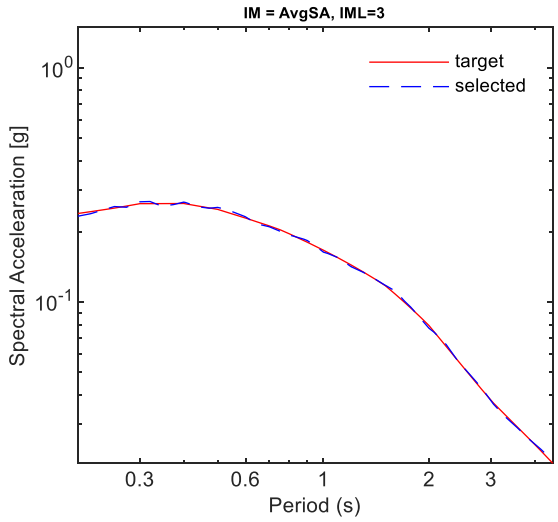

(b) target and sample means

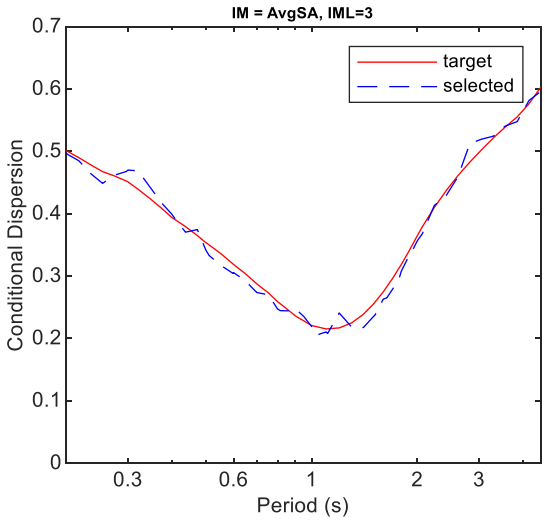

(c) target and sample standard deviations

Figure 9: 21 selected records for the 30%/50yr hazard level for Rhodes, Greece. The selected records correspond to 10 return periods.

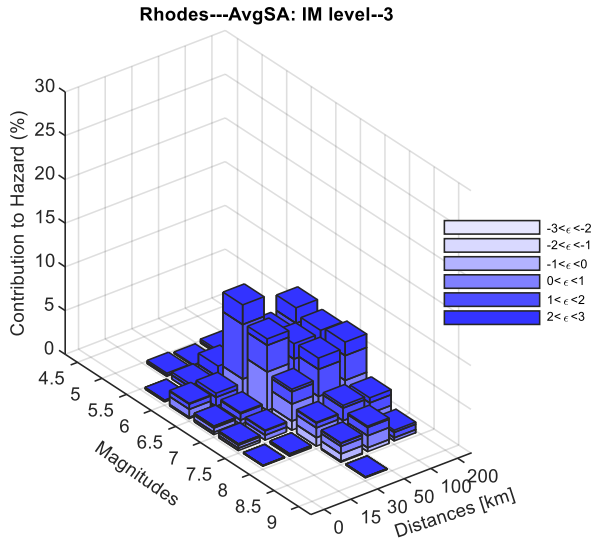

Figure 10: Disaggregation analysis results for the 30%/50yr hazard level showing the contribution of magnitude, distance and epsilon, ϵ, combinations to the seismic hazard for Rhodes, Greece.

Table 4: Names of the 21 selected records for the 30%/50yr hazard level for Rhodes.

Record names per the NGA-West [87] database		**Scale factor**
X	**Y**	
'CHICHI/TAP094-N.at2'	'CHICHI/TAP094-E.at2'	0,96
'CHICHI/TTN044-N.at2'	'CHICHI/TTN044-W.at2'	1,53
'SFERN/SBF042.at2'	'SFERN/SBF132.at2'	4,47
'CHICHI06/ILA055-N.at2'	'CHICHI06/ILA055-W.at2'	4,35
'HECTOR/11625090.at2'	'HECTOR/11625180.at2'	0,94
'CHICHI/ILA052-E.at2'	'CHICHI/ILA052-N.at2'	3,04
'NORTHR/VEN090.at2'	'NORTHR/VEN360.at2'	1,13
'CHICHI06/KAU064-N.at2'	'CHICHI06/KAU064-E.at2'	3,46
'CHICHI/CHY086-E.at2'	'CHICHI/CHY086-N.at2'	0,77
'VICT/CPE045.at2'	'VICT/CPE315.at2'	0,50
'LANDERS/SER000.at2'	'LANDERS/SER270.at2'	2,64
'CHICHI05/ILA012-N.at2'	'CHICHI05/ILA012-W.at2'	4,00
'COALINGA/H-VC2000.at2'	'COALINGA/H-VC2090.at2'	1,70
'COALINGA/H-C02000.at2'	'COALINGA/H-C02090.at2'	1,07
'DUZCE/1062-N.at2'	'DUZCE/1062-E.at2'	1,08
'CHICHI/HWA026-E.at2'	'CHICHI/HWA026-N.at2'	1,63
'CHICHI06/CHY114-N.at2'	'CHICHI06/CHY114-W.at2'	2,58
'NORTHR/TAR090.at2'	'NORTHR/TAR360.at2'	0,18
'LANDERS/FTI000.at2'	'LANDERS/FTI090.at2'	1,64
'CHICHI05/HWA041-N.at2'	'CHICHI05/HWA041-E.at2'	2,00
'HECTOR/22170090.at2'	'HECTOR/22170360.at2'	0,72

Hazard level: 10%/50yr

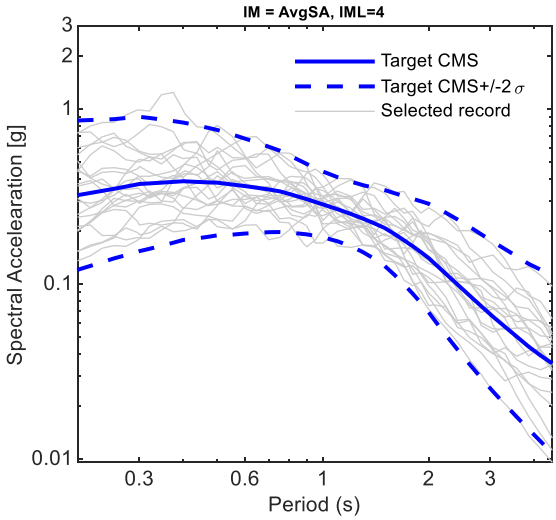

(a) response spectra

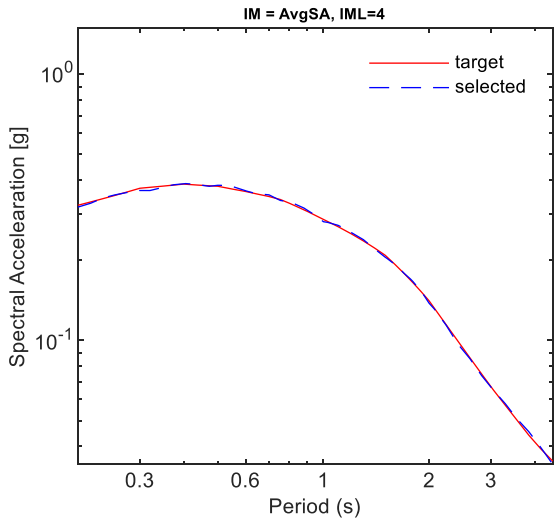

(b) target and sample means

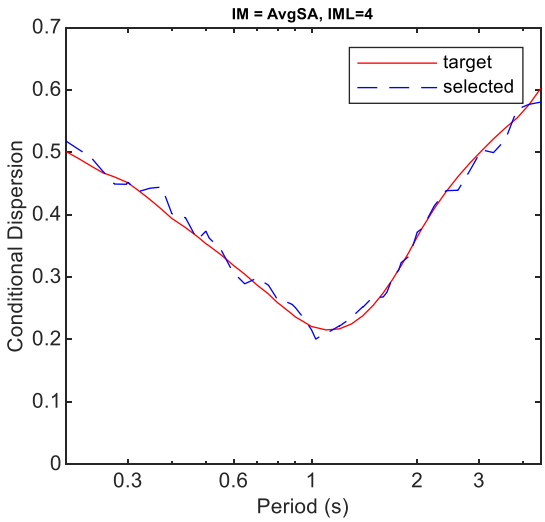

(c) target and sample standard deviations

Figure 11: 21 selected records for the 10%/50yr hazard level for Rhodes, Greece.

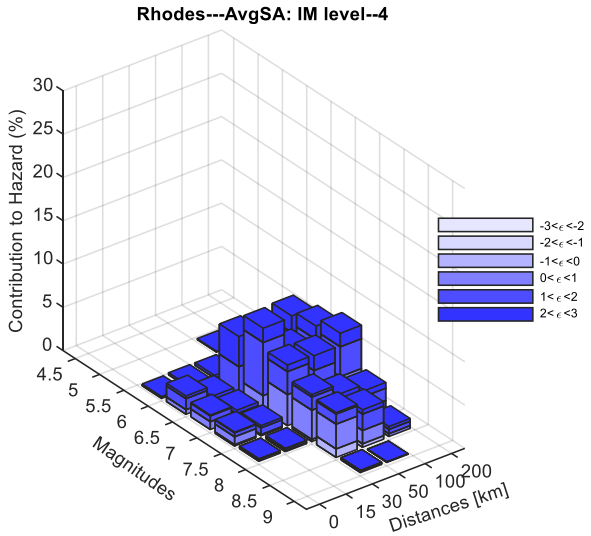

Figure 12: Disaggregation analysis results for the 10%/50yr hazard level showing the contribution of magnitude, distance and epsilon, ε, combinations to the seismic hazard for Rhodes, Greece.

Table 5: Names of the 21 selected records for the 10%/50yr hazard level for Rhodes, Greece.

Record names per the NGA-West [87] database		**Scale factor**
X	**Y**	
'NENANA/1736090.at2'	'NENANA/1736360.at2'	9,40
'CHICHI05/TTN008-N.at2'	'CHICHI05/TTN008-E.at2'	6,73
'CHICHI/CHY039-E.at2'	'CHICHI/CHY039-N.at2'	1,18
'CHICHI/TTN004-N.at2'	'CHICHI/TTN004-W.at2'	2,75
'CHICHI/STY-E.at2'	'CHICHI/STY-N.at2'	4,83
'HECTOR/11625090.at2'	'HECTOR/11625180.at2'	1,57
'CHICHI/KAU022-E.at2'	'CHICHI/KAU022-N.at2'	3,59
'CHICHI05/KAU087-N.at2'	'CHICHI05/KAU087-W.at2'	4,90
'LIVERMOR/B-FRE075.at2'	'LIVERMOR/B-FRE345.at2'	6,29
'CHICHI05/CHY088-N.at2'	'CHICHI05/CHY088-E.at2'	3,11
'CHICHI04/KAU074-N.at2'	'CHICHI04/KAU074-E.at2'	9,06
'LOMAP/DFS270.at2'	'LOMAP/DFS360.at2'	1,82
'CHICHI06/HWA014-N.at2'	'CHICHI06/HWA014-E.at2'	2,83
'CHICHI05/ILA012-N.at2'	'CHICHI05/ILA012-W.at2'	6,68
'CHICHI/ILA064-N.at2'	'CHICHI/ILA064-W.at2'	3,24
'CHICHI/CHY086-E.at2'	'CHICHI/CHY086-N.at2'	1,28
'CHICHI/KAU058-E.at2'	'CHICHI/KAU058-N.at2'	4,55
'CHICHI04/CHY052-N.at2'	'CHICHI04/CHY052-W.at2'	5,81
'NORTHR/LBR000.at2'	'NORTHR/LBR090.at2'	3,03
'NORTHR/SBG000.at2'	'NORTHR/SBG090.at2'	2,90
'KOBE/FUK000.at2'	'KOBE/FUK090.at2'	3,73

Hazard level: 2%/50yr

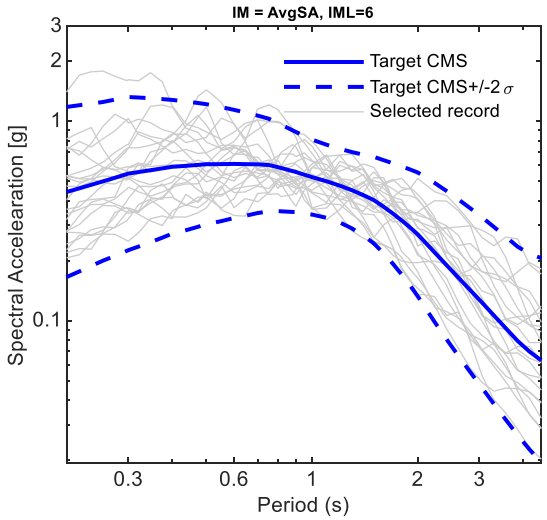

(a) response spectra

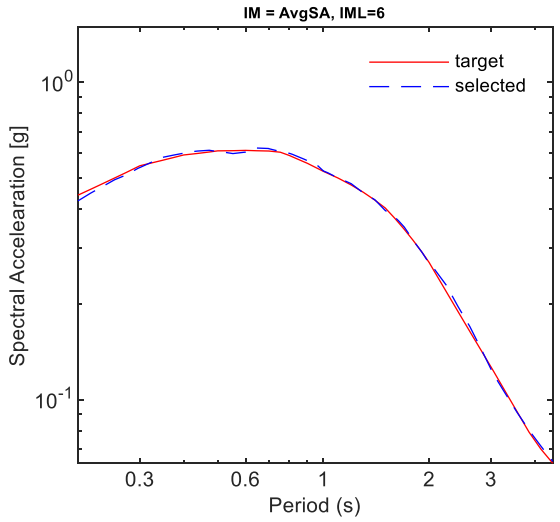

(b) target and sample means

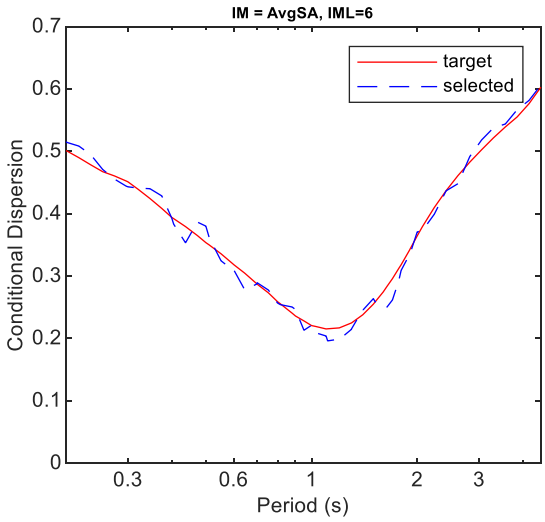

(c) target and sample standard deviations

Figure 13: 21 selected records for the 2%/50yr hazard level for Rhodes, Greece.

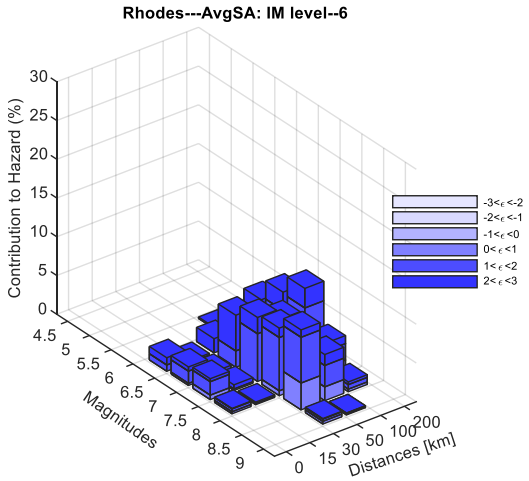

Figure 14: Disaggregation analysis results for the 2%/50yr hazard level showing the contribution of magnitude, distance and epsilon, ε, combinations to the seismic hazard for Rhodes, Greece.

Table 6: Names of the 21 selected records for the 2%/50yr hazard level for Rhodes, Greece.

Record names per the NGA-West [87] database		**Scale factor**
X	**Y**	
'CHICHI/KAU033-E.at2'	'CHICHI/KAU033-N.at2'	8,04
'CHICHI/KAU074-E.at2'	'CHICHI/KAU074-N.at2'	5,73
'CHICHI05/KAU030-N.at2'	'CHICHI05/KAU030-E.at2'	7,78
'CHICHI06/ILA007-N.at2'	'CHICHI06/ILA007-W.at2'	9,43
'CHICHI/TTN010-E.at2'	'CHICHI/TTN010-N.at2'	8,00
'CHICHI/ILA044-N.at2'	'CHICHI/ILA044-W.at2'	2,49
'CHICHI/KAU022-E.at2'	'CHICHI/KAU022-N.at2'	6,39
'CHICHI/KAU073-E.at2'	'CHICHI/KAU073-N.at2'	6,28
'LOMAP/OLEM000.at2'	'LOMAP/OLEM090.at2'	2,39
'ITALY/A-TRC000.at2'	'ITALY/A-TRC270.at2'	7,98
'CHICHI06/KAU012-N.at2'	'CHICHI06/KAU012-E.at2'	8,89
'CHICHI05/TTN009-N.at2'	'CHICHI05/TTN009-E.at2'	10,00
'SMART1/25E01EW.at2'	'SMART1/25E01NS.at2'	9,08
'HECTOR/1442c090.at2'	'HECTOR/1442a360.at2'	7,94
'KOBE/TAZ000.at2'	'KOBE/TAZ090.at2'	0,51
'CHICHI/CHY086-E.at2'	'CHICHI/CHY086-N.at2'	2,28
'CHICHI/HSN-E.at2'	'CHICHI/HSN-N.at2'	3,06
'CHICHI03/CHY041-N.at2'	'CHICHI03/CHY041-E.at2'	5,34
'HECTOR/0292c090.at2'	'HECTOR/0292a360.at2'	9,58
'KOBE/KJM000.at2'	'KOBE/KJM090.at2'	0,51
'CHICHI06/TTN044-N.at2'	'CHICHI06/TTN044-W.at2'	8,11

Granada

Hazard level: 30%/50yr

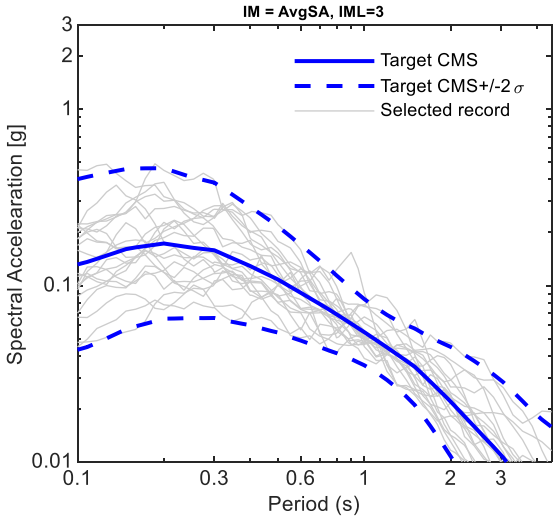

(a) response spectra

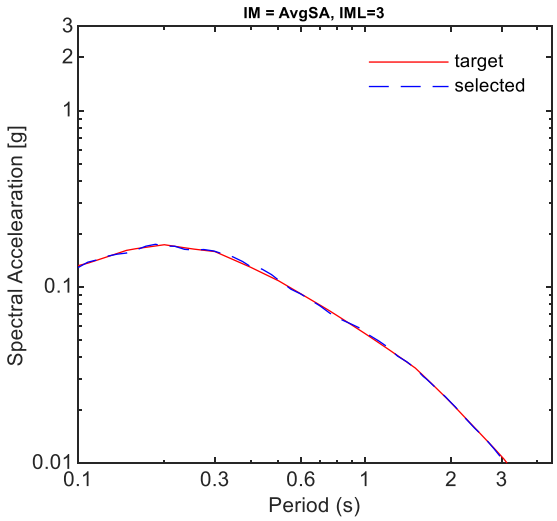

(b) target and sample means

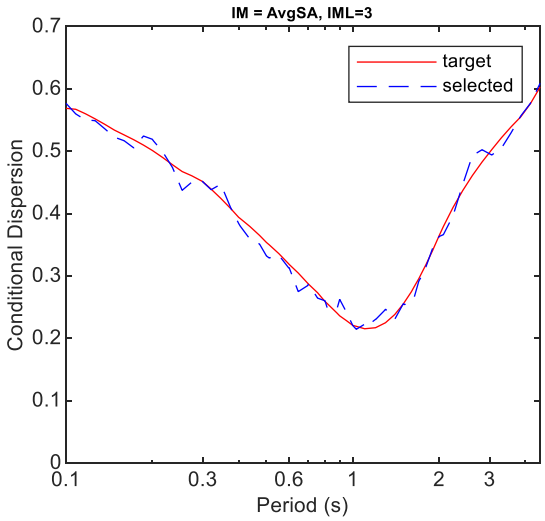

(c) target and sample standard deviations

Figure 15: 21 selected records for the 30%/50yr hazard level for Granada, Spain. The selected records correspond to 10 return periods.

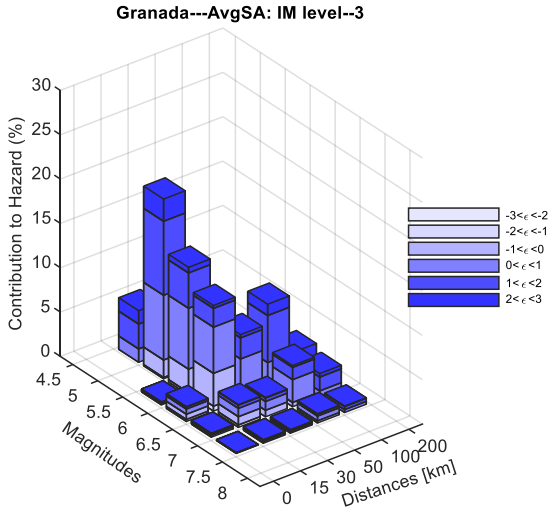

Figure 16: Disaggregation analysis results for the 30%/50yr hazard level showing the contribution of magnitude, distance and epsilon, ε, combinations to the seismic hazard for Granada, Spain.

Table 7: Names of the 21 selected records for the 30%/50yr hazard level for Granada, Spain.

Record names per the NGA-West [87] database		**Scale factor**
X	**Y**	
'LANDERS/OBR000.at2'	'LANDERS/OBR090.at2'	0,61
'CHICHI04/CHY080-N.at2'	'CHICHI04/CHY080-E.at2'	0,41
'CHICHI05/TTN014-N.at2'	'CHICHI05/TTN014-E.at2'	1,55
'CHICHI/ILA050-E.at2'	'CHICHI/ILA050-N.at2'	0,78
'SMART1/33O07EW.at2'	'SMART1/33O07NS.at2'	1,70
'CHICHI03/TCU067-N.at2'	'CHICHI03/TCU067-E.at2'	0,48
'HECTOR/22170090.at2'	'HECTOR/22170360.at2'	0,25
'CHICHI06/CHY025-N.at2'	'CHICHI06/CHY025-E.at2'	0,31
'WHITTIER/A-BLD000.at2'	'WHITTIER/A-BLD090.at2'	0,66
'IMPVALL/H-VCT075.at2'	'IMPVALL/H-VCT345.at2'	0,79
'NORTHR/STM090.at2'	'NORTHR/STM360.at2'	0,14
'CHICHI05/HWA003-N.at2'	'CHICHI05/HWA003-W.at2'	2,20
'CHICHI06/CHY019-N.at2'	'CHICHI06/CHY019-W.at2'	1,17
'WHITTIER/A-CWC180.at2'	'WHITTIER/A-CWC270.at2'	0,61
'NORTHR/LAC090.at2'	'NORTHR/LAC180.at2'	0,34
'NORTHR/DWN090.at2'	'NORTHR/DWN360.at2'	0,35
'CHICHI06/CHY029-N.at2'	'CHICHI06/CHY029-E.at2'	0,33
'NORTHR/5081-360.at2'	'NORTHR/5081-270.at2'	0,52
'CABAJA/2028a090.at2'	'CABAJA/2028b360.at2'	1,90
'LIVERMOR/B-A3E146.at2'	'LIVERMOR/B-A3E236.at2'	2,26
'HECTOR/12331360.at2'	'HECTOR/12331090.at2'	0,83

Hazard level: 10%/50yr

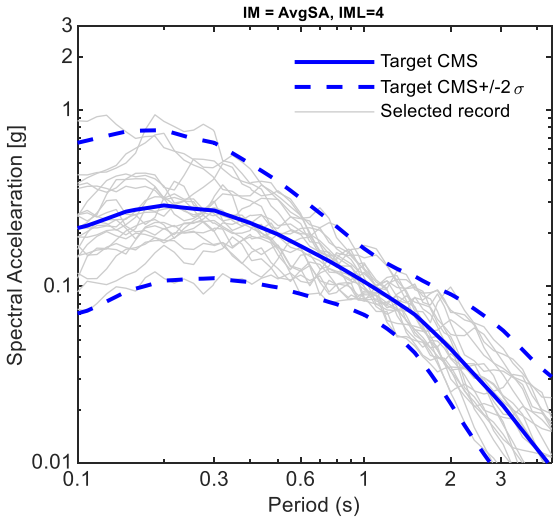

(a) response spectra

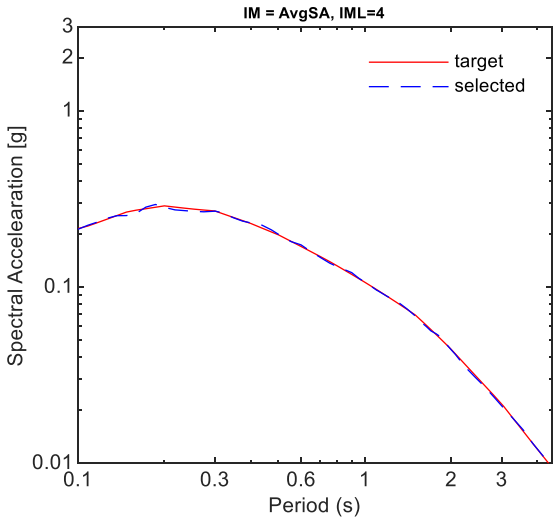

(b) target and sample means

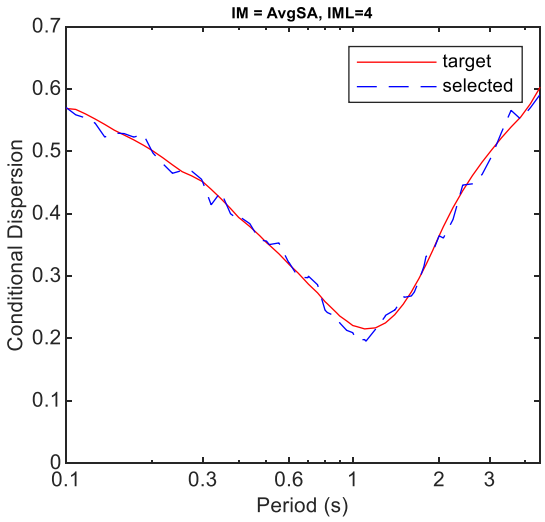

(c) target and sample standard deviations

Figure 17: 21 selected records for the 10%/50yr hazard level for Granada, Spain.

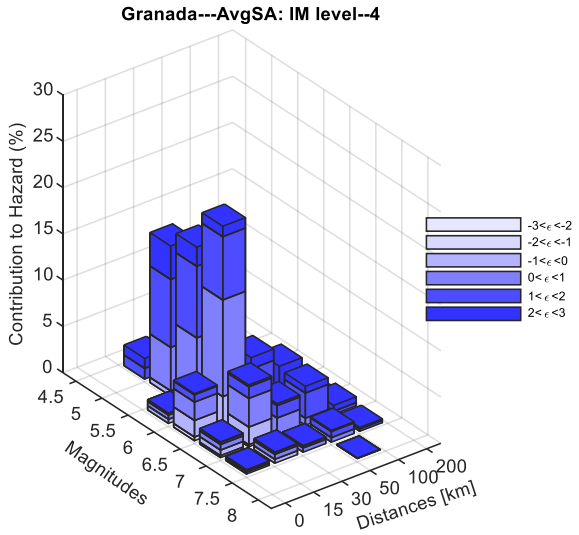

Figure 18: Disaggregation analysis results for the 10%/50yr hazard level showing the contribution of magnitude, distance and epsilon, ε, combinations to the seismic hazard for Granada, Spain.

Table 8: Names of the 21 selected records for the 10%/50yr hazard level for Granada.

Record names per the NGA-West [87] database		Scale factor
X	Y	
'LANDERS/JAB220.at2'	'LANDERS/JAB310.at2'	1,37
'CHICHI04/TCU038-N.at2'	'CHICHI04/TCU038-E.at2'	3,70
'LOMAP/FMS090.at2'	'LOMAP/FMS180.at2'	0,75
'IMPVALL/I-ELC180.at2'	'IMPVALL/I-ELC270.at2'	0,32
'NORTHR/0637-270.at2'	'NORTHR/0637-360.at2'	0,15
'KOCAELI/ATK000.at2'	'KOCAELI/ATK090.at2'	0,70
'CHICHI04/TTN022-N.at2'	'CHICHI04/TTN022-E.at2'	2,63
'MANJIL/188040.at2'	'MANJIL/188310.at2'	0,68
'WHITTIER/B-BLD000.at2'	'WHITTIER/B-BLD090.at2'	1,47
'LOMAP/SJTE225.at2'	'LOMAP/SJTE315.at2'	0,49
'IMPVALL/H-E13140.at2'	'IMPVALL/H-E13230.at2'	0,84
'CHICHI04/HWA005-N.at2'	'CHICHI04/HWA005-W.at2'	3,20
'SFERN/PDL120.at2'	'SFERN/PDL210.at2'	0,69
'WHITTIER/A-RO2090.at2'	'WHITTIER/A-RO2180.at2'	1,29
'IMPVALL/H-VCT075.at2'	'IMPVALL/H-VCT345.at2'	1,52
'NORTHR/STN020.at2'	'NORTHR/STN110.at2'	0,32
'CHICHI05/CHY115-N.at2'	'CHICHI05/CHY115-W.at2'	2,22
'NORTHR/5081-360.at2'	'NORTHR/5081-270.at2'	0,99
'CABAJA/2028a090.at2'	'CABAJA/2028b360.at2'	3,64
'WHITTIER/A-FAI000.at2'	'WHITTIER/A-FAI270.at2'	0,90
'MORGAN/HD4345.at2'	'MORGAN/HD4255.at2'	0,82

Hazard level: 2%/50yr

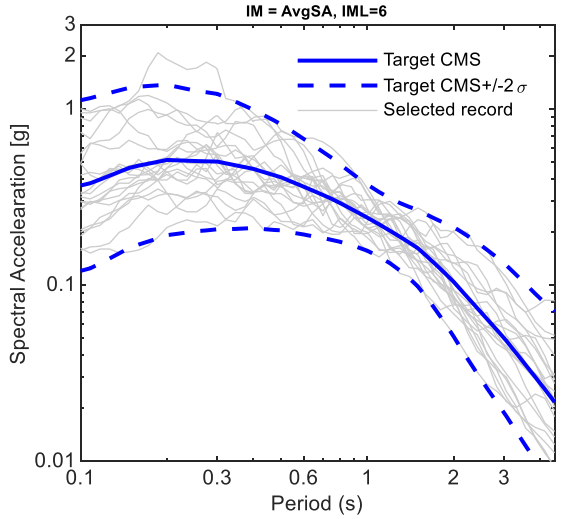

(a) response spectra

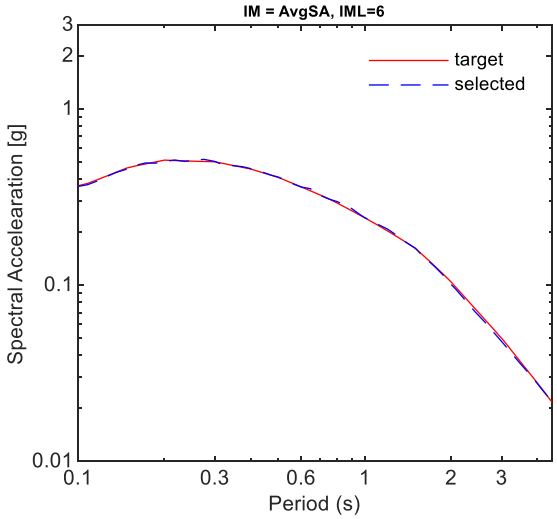

(b) target and sample means

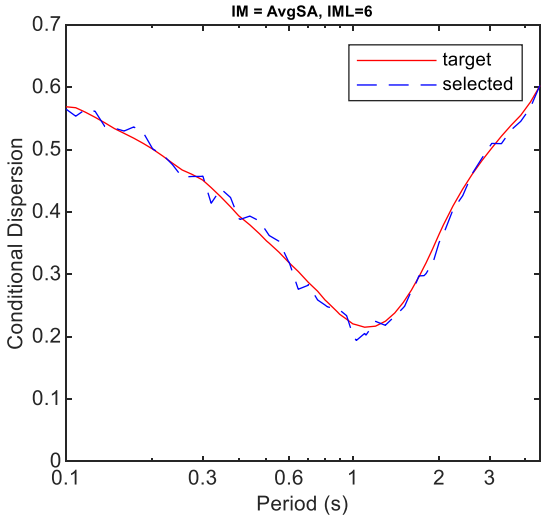

(c) target and sample standard deviations

Figure 19: 21 selected records for the 2%/50yr hazard level for Granada, Spain.

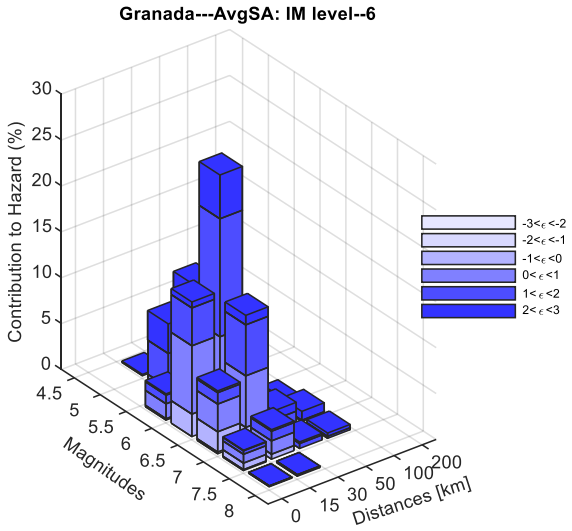

Figure 20: Disaggregation analysis results for the 2%/50yr hazard level showing the contribution of magnitude, distance and epsilon, ε, combinations to the seismic hazard for Granada, Spain.

Table 9: Names of the 21 selected records for the 2%/50yr hazard level for Granada.

Record names per the NGA-West [87] database		Scale factor
X	Y	
'LOMAP/PHT270.at2'	'LOMAP/PHT360.at2'	2,35
'NORTHR/LDM064.at2'	'NORTHR/LDM334.at2'	0,43
'CHICHI/CHY057-E.at2'	'CHICHI/CHY057-N.at2'	3,73
'CHICHI/HWA026-E.at2'	'CHICHI/HWA026-N.at2'	2,44
'NORTHR/PIC090.at2'	'NORTHR/PIC180.at2'	1,65
'CHICHI03/TCU120-N.at2'	'CHICHI03/TCU120-E.at2'	1,93
'HECTOR/HEC000.at2'	'HECTOR/HEC090.at2'	0,63
'BORREGO/A-ELC180.at2'	'BORREGO/A-ELC270.at2'	1,55
'WHITTIER/A-JAB207.at2'	'WHITTIER/A-JAB297.at2'	1,28
'BAJA/CPE161.at2'	'BAJA/CPE251.at2'	0,42
'ITALY/B-VLT000.at2'	'ITALY/B-VLT270.at2'	1,87
'CHICHI06/TCU052-N.at2'	'CHICHI06/TCU052-E.at2'	2,85
'LOMAP/A2E000.at2'	'LOMAP/A2E090.at2'	1,22
'SMART1/05O07EW.at2'	'SMART1/05O07NS.at2'	2,45
'PALMSPR/DSP000.at2'	'PALMSPR/DSP090.at2'	1,03
'CHICHI06/CHY041-N.at2'	'CHICHI06/CHY041-E.at2'	1,43
'LANDERS/OBR000.at2'	'LANDERS/OBR090.at2'	2,59
'NORTHR/5081-360.at2'	'NORTHR/5081-270.at2'	2,19
'LOMAP/GIL067.at2'	'LOMAP/GIL337.at2'	1,11
'NORTHR/FIG058.at2'	'NORTHR/FIG328.at2'	2,09
'MORGAN/SJR270.at2'	'MORGAN/SJR360.at2'	2,84

4. Conclusions

In the present deliverable, advanced and reliable modelling for a broad spectrum of natural and man-made hazards was presented, in order to provide the involved stakeholders, scientists and users with useful information for their specific needs in handling natural and human induced disasters. The models that were presented included the atmospheric models and the seismic models.

Concerning the atmospheric models, the scientific progress of the atmospheric models from the moment of their appearance until today was significant. The main definition of an atmospheric model is that it is a mathematical model constructed around the full set of primitive dynamical equations which govern atmospheric motions. It can supplement these equations with parameterizations for turbulent diffusion, radiation, moist processes (clouds and precipitation), heat exchange, soil, vegetation, surface water, the kinematic effects of terrain, and convection. Most atmospheric models are numerical, i.e. they discretize equations of motion. They can predict microscale phenomena such as tornadoes and boundary layer eddies, sub-microscale turbulent flow over buildings, as well as synoptic and global flows. The horizontal domain of a model is either global, covering the entire Earth, or regional (limited-area), covering only part of the Earth. The different types of models run are thermotropic, barotropic, hydrostatic, and nonhydrostatic. Some of the model types make assumptions about the atmosphere which lengthens the time steps used and increases computational speed.

Forecasts are computed using mathematical equations for the physics and dynamics of the atmosphere. These equations are nonlinear and are impossible to solve exactly. Therefore, numerical methods obtain approximate solutions. Different models use different solution methods. Global models often use spectral methods for the horizontal dimensions and finite-difference methods for the vertical dimension, while regional models usually use finite-difference methods in all three dimensions. For specific locations, model output statistics use climate information, output from numerical weather prediction, and current surface weather observations to develop statistical relationships which account for model bias and resolution issues. For the needs of the Working Package 3 of the HYPERION project the atmospheric model PALM was used a description of which is given in Section 2.9.

Concerning the seismic models, they employ the state-of-the-art data of the European Seismic Hazard Model (ESHM13), as well as cutting edge methodologies of Conditional Spectra, advanced Intensity Measures, event-based Probabilistic Seismic Hazard Assessment and spatially-correlated ground motion fields to deliver: (a) Wide area consistent seismic source models and earthquake rupture forecasts, (b) spatially consistent scenarios of ground motion fields, (c) cross-correlated Intensity Measure values at each location of interest, and (d) a hazard-consistent set of ground motion records that can be employed to deliver site-specific fragility and vulnerability functions for each asset of interest. All in all, these allow the accurate and unbiased seismic risk assessment of interconnected historic areas, and combined with weather models offer an integrated view of the overall system resilience.

5. References

[1] Pielke, Roger A. (2002). Mesoscale Meteorological Modelling. Academic Press. pp. 48–49. ISBN 978-0-12-554766-6.

[2] Pielke, Roger A. (2002). Mesoscale Meteorological Modelling. Academic Press. pp. 285–287. ISBN 978-0-12-554766-6.

[3] Sunderam, V. S.; G. Dick van Albada; Peter M. A. Sloot; J. J. Dongarra (2005). Computational Science – ICCS 2005: 5th International Conference, Atlanta, GA, USA, May 22–25, 2005, Proceedings, Part 1. Springer. p. 132. ISBN 978-3-540-26032-5.

[4] Zwieflhofer, Walter; Norbert Kreitz; European Centre for Medium Range Weather Forecasts (2001). Developments in teracomputing: proceedings of the ninth ECMWF Workshop on the Use of High Performance Computing in Meteorology. World Scientific. p. 276. ISBN 978-981-02-4761-4.

[5] Chan, Johnny C. L. & Jeffrey D. Kepert (2010). Global Perspectives on Tropical Cyclones: From Science to Mitigation. World Scientific. pp. 295–301. ISBN 978-981-4293-47-1.

[6] Holton, James R. (2004). An introduction to dynamic meteorology, Academic Press. p. 480. ISBN 978-0-12-354015-7.

[7] Brown, Molly E. (2008). Famine early warning systems and remote sensing data. Springer. p. 121. ISBN 978-3-540-75367-4.

[8] Strikwerda, John C. (2004). Finite difference schemes and partial differential equations. SIAM. pp. 165–170. ISBN 978-0-89871-567-5.

[9] Pielke, Roger A. (2002). Mesoscale Meteorological Modelling. Academic Press. p. 65. ISBN 978-0-12-554766-6.

[10] C. Donald Ahrens, Robert Henson (2018). Essentials of Meteorology: An Invitation to the Atmosphere, 8th Edition. Cengage. ISBN 978-1-305-62845-8.

[11] Gates, W. Lawrence; Leon S. Pocinki; Carl F. Jenkins, (1955). Results Of Numerical Forecasting With The Barotropic And Thermotropic Atmospheric Models. Geophysics Research Directorate, Air Force Cambridge Research Center, Bedford Massachusetts.

[12] Thompson, P. D.; W. Lawrence Gates (1956). "A Test of Numerical Prediction Methods Based on the Barotropic and Two-Parameter Baroclinic Models". Journal of Meteorology. 13 (2): 127–141.

[13] Wallace, John M. & Peter V. Hobbs (2006). Atmospheric Science: An Introductory Survey. Academic Press, Inc. ISBN 978-0-12-732951-2.

[14] Marshall, John; Plumb, R. Alan (2007). Atmosphere, Ocean and Climate Dynamics. Elsevier Academic Press. ISBN 978-0-08-055670-3.

[15] Charney, Jule; Fjörtoft, Ragnar; von Neumann, John (1950). "Numerical Integration of the Barotropic Vorticity Equation". Tellus. 2 (4): 237–254.

[16] Jacobson, Mark Zachary (2005). Fundamentals of atmospheric modelling. Cambridge University Press. pp. 138–143. ISBN 978-0-521-83970-9.

[17] Lynch, Peter (2008). "The origins of computer weather prediction and climate modelling". Journal of Computational Physics. 227 (7): 3431–44.

[18] Lynch, Peter (2014). The Emergence of Numerical Weather Prediction: Richardson's Dream. Cambridge University Press. ISBN 978-1-107-41483-9.

[19] Cox, John D. (2002). Storm Watchers. John Wiley & Sons, Inc. p. 208. ISBN 978-0-471-38108-2.

[20] Harper, Kristine; Uccellini, Louis W.; Kalnay, Eugenia; Carey, Kenneth; Morone, Lauren (2007). "50th Anniversary of Operational Numerical Weather Prediction". Bulletin of the American Meteorological Society. 88 (5): 639–650.

[21] Leslie, L.M.; Dietachmayer, G.S. (1992). "Real-time limited area numerical weather prediction in Australia: a historical perspective". Australian Meteorological Magazine. 41: 61–77.

[22] Norman A. Phillips (1956). "The general circulation of the atmosphere: a numerical experiment". Quarterly Journal of the Royal Meteorological Society. 82 (352): 123–164.

[23] John D. Cox (2002). Storm Watchers. John Wiley & Sons, Inc. p. 210. ISBN 978-0-471-38108-2.

[24] Shuman, Frederick G. (1989). "History of Numerical Weather Prediction at the National Meteorological Center". Weather and Forecasting. 4 (3): 286–296.

[25] Van Dop, H., Steyn, Douw G., (1991). Air pollution modelling and its application VIII, Springer. pp. 241–242. ISBN 978-0-306-43828-8.

[26] https://en.wikipedia.org/wiki/Model_output_statistics.

[27] J. Struzewska, J.W. Kaminski, M. Jefimow, (2016). Application of model output statistics to the GEM-AQ high resolution air quality forecast. Atmospheric Research, 181, 186–199.

[28] Cox, John D. (2002). Storm Watchers. John Wiley & Sons, Inc. pp. 222–224. ISBN 978-0-471-38108-2.

[29] https://en.wikipedia.org/wiki/Ensemble_forecasting.

[30] Toth, Zoltan; Kalnay, Eugenia (1997). "Ensemble Forecasting at NCEP and the Breeding Method". Monthly Weather Review. 125 (12): 3297–3319.

[31] https://www.ecmwf.int/ (European Centre for Medium-Range Weather Forecasts).

[32] Molteni, F.; Buizza, R.; Palmer, T.N.; Petroliagis, T. (1996). "The ECMWF Ensemble Prediction System: Methodology and validation". Quarterly Journal of the Royal Meteorological Society. 122: 73–119.

[33] Stensrud, David (2007). Parameterization schemes: keys to understanding numerical weather prediction models. Cambridge University Press. p. 56. ISBN 978-0-521-86540-1.

[34] https://en.wikipedia.org/wiki/METAR.

[35] https://vest.agrisemantics.org/content/synop-data-format-fm-12-surface-synoptic-observations.

[36] Kwon, J. H. et al., (2007). Parallel computational fluid dynamics: parallel computing and its applications: Proceedings of the Parallel CFD 2006 Conference, Busan city, Korea (May 15–18, 2006). Elsevier. p. 224. ISBN 978-0-444-53035-6.

[37] https://en.wikipedia.org/wiki/Data_assimilation.

[38] https://en.wikipedia.org/wiki/Radiosonde.

[39] http://amdar.noaa.gov/docs/bams_ballish_kumar.pdf.

[40] https://www.vos.noaa.gov/vos_scheme.shtml.

[41] 403rd Wing (2011). "The Hurricane Hunters". 53rd Weather Reconnaissance Squadron.

[42] https://en.wikipedia.org/wiki/53rd_Weather_Reconnaissance_Squadron.

[43] https://en.wikipedia.org/wiki/Reconnaissance_aircraft.

[44] Stensrud, David J. (2009). Parameterization schemes: keys to understanding numerical weather prediction models. Cambridge University Press. ISBN 978-0-521-12676-2.

[45] https://en.wikipedia.org/wiki/History_of_numerical_weather_prediction.

[46] Narita, Masami & Shiro Ohmori (2007). "3.7 Improving Precipitation Forecasts by the Operational Nonhydrostatic Mesoscale Model with the Kain-Fritsch Convective Parameterization and Cloud Microphysics". 12th Conference on Mesoscale Processes. American Meteorological Society.

[47] Frierson, Dargan (2000). "The Diagnostic Cloud Parameterization Scheme". University of Washington. pp. 4–5 (https://web.archive.org/web/20110401013742/http://www.atmos.washington.edu/~dargan/591/diag_cloud.tech.pdf).

[48] Stensrud, David J. (2007). Parameterization schemes: keys to understanding numerical weather prediction models. Cambridge University Press. p. 6. ISBN 978-0-521-86540-1.

[49] Mel'nikova, Irina N. & Alexander V. Vasilyev (2005). Short-wave solar radiation in the earth's atmosphere: calculation, oberservation, interpretation. Springer. ISBN 978-3-540-26692-1.

[50] Stensrud, David J. (2007). Parameterization schemes: keys to understanding numerical weather prediction models. Cambridge University Press. pp. 12–14. ISBN 978-0-521-86540-1.

[51] Warner, Thomas Tomkins (2010). Numerical Weather and Climate Prediction. Cambridge University Press. p. 259. ISBN 978-0-521-51389-0.

[52] Lynch, Peter (2014). The Emergence of Numerical Weather Prediction: Richardson's Dream. Cambridge University Press. ISBN 978-1-107-41483-9.

[53] C. Donald Ahrens, Robert Henson (2018). Essentials of Meteorology: An Invitation to the Atmosphere, 8th Edition. Cengage. ISBN 978-1-305-62845-8.

[54] Janjic, Zavisa; Gall, Robert; Pyle, Matthew E. (2010). "Scientific Documentation for the NMM Solver". National Center for Atmospheric Research. pp. 12–13.

[55] http://www.cosmo-model.org/content/model/general/default.htm.

[56] Lac, C., Chaboureau, P., Masson, V., Pinty, P., Tulet, P., Escobar, J., et al., (2018). Overview of the Meso-NH model version 5.4 and its applications. Geoscientific Model Development, 11, 1929-1969.

[57] Lafore, Jean Philippe, et al., (1997). "The Meso-NH atmospheric simulation system. Part I: Adiabatic formulation and control simulations." Annales geophysicae. Vol. 16.

[58] Baum, Marsha L. (2007). When nature strikes: weather disasters and the law. Greenwood Publishing Group. p. 189. ISBN 978-0-275-22129-4.

[59] Gultepe, Ismail (2007). Fog and boundary layer clouds: fog visibility and forecasting. Springer. ISBN 978-3-7643-8419-7.

[60] Barry, Roger Graham & Richard J. Chorley (2003). Atmosphere, weather, and climate. Psychology Press. ISBN 978-0-415-27170-7.

[61] Lynch, Peter (2014). The Emergence of Numerical Weather Prediction: Richardson's Dream. Cambridge University Press. ISBN 978-1-107-41483-9.

[62] https://en.wikipedia.org/wiki/History_of_numerical_weather_prediction.

[63] "CAM 3.1 Download". www.cesm.ucar.edu.

[64] William D. Collins; et al. (2004). "Description of the NCAR Community Atmosphere Model (CAM 3.0)". University Corporation for Atmospheric Research.

[65] "CAM3.0 COMMUNITY ATMOSPHERE MODEL". https://www.cesm.ucar.edu/models/atm-cam/.

[66] Yongkang Xue & Michael J. Fennessey (1996). "Impact of vegetation properties on U. S. summer weather prediction". Journal of Geophysical Research. 101 (D3): 7419-7430.

[67] Alexander Baklanov; Alix Rasmussen; Barbara Fay; Erik Berge; Sandro Finardi (2002). "Potential and Shortcomings of Numerical Weather Prediction Models in Providing Meteorological Data for Urban Air Pollution Forecasting". Water, Air, & Soil Pollution: Focus. 2: 43–60. doi:10.1023/A:1021394126149.

[68] "National Hurricane Center Forecast Verification". National Hurricane Center, https://www.nhc.noaa.gov/verification/.

[69] Edward N. Rappaport et al., (2009). "Advances and Challenges at the National Hurricane Center". Weather and Forecasting. 24 (2): 395–419.

[70] Cornell CA (1968): Engineering Seismic Risk Analysis. Bulletin of the Seismological Society of America 58, 1583-1606.

[71] Bazzurro P, Cornell CA (1999): Disaggregation of Seismic Hazard. Bulletin of the Seismological Society of America, 89(2), 501-520.

[72] McGuire RK (2007): Probabilistic seismic hazard analysis: Early history. Earthquake Engineering & Structural Dynamics, 37(3), 329-338.

[73] PANOPTIS Consortium (2020): D4.7: D4.3.2 Multi-Hazard Vulnerability Modules for RI and related non-RI elements – V2.

[74] Baker JW (2013): Probabilistic Seismic Hazard Analysis. White Paper Version 2.0.1, 79 pp.

[75] Pagani M, Monelli D, Weatherill GA, Garcia J (2014): The OpenQuake-engine Book: Hazard. Global Earthquake Model (GEM) Technical Report 2014-08, doi: 10.13117/-GEM.OPENQUAKE.TR2014.08.

[76] Lin T, Haselton CB, Baker JW (2013): Conditional spectrum-based ground motion selection. Part I: Hazard consistency for risk-based assessments. Earthquake Engineering and Structural Dynamics 42(12), 1847-1865. DOI: 10.1002/eqe.2301.

[77] Kohrangi M, Bazzurro P, Vamvatsikos D, Spillatura A (2017): Conditional spectrum based ground motion record selection using average spectral acceleration. Earthquake Engineering and Structural Dynamics, 46(10):1667-1685. DOI: 10.1002/eqe.2876.

[78] Kohrangi M. (2015): Beyond simple scalar ground motion intensity measures for seismic risk assessment. PhD Thesis, University of Pavia, Italy.

[79] GEM (2020): The OpenQuake-engine User Manual. Global Earthquake Model (GEM) OpenQuake Manual for Engine version 3.10.1. doi: 10.13117/GEM.OPENQUAKE.MAN.ENGINE.3.10.1.

[80] Giardini, D., Woessner, J., Danciu, L., Crowley, H., Cotton, F., Grünthal, G., et al, 2013. Seismic Hazard Harmonization in Europe (SHARE): Online Data Resource, http://www.share-eu.org/node/61.html, doi: 10.12686/SED-00000001-SHARE, 2013.

[81] Woessner, J., Danciu, L., Giardini, D., Crowley, H., Cotton, F., Grünthal, G. et al, 2015. The 2013 European seismic hazard model: key components and results. Bulletin of Earthquake Engineering 13(12): 3553–3596.

[82] Hiemer, S., Jackson, D.D., Wang, Q. et al., 2013. A stochastic forecast of California earthquakes based on fault slip and smoothed seismicity. Bulletin of the Seismological Society of America, 103(2A): 799–810. doi:10.1785/0120120168.

[83] Boore DM, Atkinson GM (2008): Ground-Motion Prediction Equations for the Average Horizontal Component of PGA, PGV, and 5%-Damped PSA at Spectral Periods between 0.01 s and 10.0 s. Earthquake Spectra, 24 (1), 99-138.

[84] Cordova P, Deierlein G, Mehanny SF, Cornell CA (2001): Development of a two-parameter seismic intensity measure and probabilistic assessment procedure. The Second U.S.-Japan Workshop on Performance-Based Earthquake Engineering Methodology for Reinforced Concrete Building Structures, Sapporo, Hokkaido, Japan.

[85] Vamvatsikos D, Cornell CA (2005): Developing efficient scalar and vector intensity measures for IDA capacity estimation by incorporating elastic spectral shape information. Earthquake Engineering and Structural Dynamics, 34(13), 1573-1600.

[86] Kazantzi AK, Vamvatsikos D (2015): Intensity measure selection for vulnerability studies of building classes. Earthquake Engineering and Structural Dynamics 44(15), 2677-2694.

[87] Ancheta, T.D., Darragh, R.B., Stewart, J.P., Seyhan, E., Silva, W.J., Chiou, B.S.J., Wooddell, K.E., Graves, R.W., Kottke, A.R., Boore, D.M. and Kishida, T., 2014. NGA-West2 database. Earthquake Spectra, 30(3), 989-1005.